Human Type-α Transforming Growth Factor Undergoes Slow Conformational Exchange between Multiple Backbone Conformations As Characterized by Nitrogen-15 Relaxation Measurements†

Yu-Chin Li and Gaetano T. Montelione*

Center for Advanced Biotechnology and Medicine, Department of Molecular Biology and Biochemistry, and The Graduate Program in Chemistry, Rutgers University, Piscataway, New Jersey 08854-5638

Received August 5, 1994; Revised Manuscript Received November 28, 1994⊗

ABSTRACT: Human type-α transforming growth factor (hTGFα) is a small mitogenic protein containing 50 amino acids and three disulfide bonds. It has both sequence and structural homology with epidermal growth factor (EGF). While the three-dimensional structures of hTGFα and other EGF-like proteins have been studied extensively, relatively little is known about conformational dynamics of these molecules. In this paper we describe nuclear relaxation measurements which probe the molecular dynamics of hTGFα in aqueous solution at neutral pH. In order to characterize conformational dynamics of hTGFα on both the fast (i.e., sub-nanosecond) and intermediate nitrogen-15 chemical-exchange (i.e., microsecond) time scales, we measured nitrogen-15 relaxation parameters at pH 7.1 ± 0.1 and a temperature of 30 ± 0.5 °C. Measurements of nitrogen-15 longitudinal (R_1) and transverse (R_2) relaxation rates, and $^1H-^{15}N$ heteronuclear NOE effects, were then interpreted using an extended Lipari−Szabo analysis [Lipari, G., & Szabo, A. (1982) *J. Am. Chem. Soc. 104,* 4546−4559; Clore, G. M., Szabo, A., Bax, A., Kay, L. E., Driscoll, P. C., & Gronenborn, A. M. (1990) *J. Am. Chem. Soc. 112,* 4989−4991] to provide estimates of the locations and amplitudes of fast internal motions and the locations of nitrogen-15 chemical-exchange line broadening. These results demonstrate that, under conditions of pH and temperature at which it is tightly bound by the EGF receptor, hTGFα is a highly dynamic molecule. Indeed, some 40% of the backbone amide groups of hTGFα, including many at the interface between the two subdomains, exhibit significant nitrogen-15 chemical-exchange line broadening indicative of interconversions between multiple protein conformations on the microsecond time scale. The distribution of these sites on the three-dimensional protein structure suggests that these dynamic fluctuations are due to (i) partial unfolding of the core β-sheet, (ii) hinge-bending motions between the N- and C-terminal subdomains, and/or (iii) disulfide bond isomerization in the solution structure of hTGFα at neutral pH.

Human type-α transforming growth factor (hTGFα)[1] is a small mitogenic protein containing 50 amino acids and three disulfide bonds (Roberts et al., 1980; Marquardt et al., 1983; Derynck et al., 1984). It has both sequence and structural homology with epidermal growth factor (EGF) (Simpson et al., 1985; Campbell & Bork, 1993), competes with EGF for binding the same membrane-bound receptor (Carpenter et al., 1983), and acts synergistically with other growth factors, including type-β transforming growth factor (TGFβ), to induce phenotypic transformation in certain cells lines (Roberts et al., 1981; Anzano et al., 1983; Guerin et al., 1989). TGFα and other EGF-like proteins also play central roles in the molecular basis of wound healing (Burgess, 1989; Jyung & Mustoe, 1992) and in the etiology of some human cancers (Burgess, 1989; Guerin et al., 1989).

NMR solution structures have been described for hTGFα (Brown et al., 1989; Kohda et al., 1989; Montelione et al., 1989, Tappin et al., 1989; Kline et al., 1990; Harvey et al., 1991; Moy et al., 1993) and for several homologous proteins including human EGF (hEGF) (Carver et al., 1986; Cooke et al., 1987; Hommel et al., 1992), murine EGF (mEGF) (Montelione et al., 1986, 1987, 1992; Kohda & Inagaki, 1988, 1992a; Kohda et al., 1988), micelle-bound mEGF (Kohda & Inagaki, 1992b), rat EGF (Mayo et al., 1989), and the EGF-like domains from bovine coagulation factor X (Selander et al., 1990; Ullner et al., 1992), human factor IX (Huang et al., 1991; Baron et al., 1992), human tissue-type plasminogen activator (Smith et al., 1994), and human urokinase-type plasminogen activator (Hansen et al., 1994). X-ray crystal structures of the EGF-like domains of human E-selectin (Graves et al., 1994; Weis, 1994) and human factor Xa (Padmanabhan et al., 1993) have also been determined recently. All of these EGF-like molecules or domains have

† This work was supported by the National Institutes of Health (GM-47014), by the National Science Foundation (MCB-9407569 and NSF Young Investigator Award MCB-9357526), and by an American Cyanamid Award in Physical and Analytical Chemistry.

* Correspondence should be addressed to this author at CABM, Rutgers University, 679 Hoes Lane, Piscataway, NJ 08854-5638 (telephone 908-235-5321; FAX 908-235-4850; e.mail guy@nmrlab.cabm.rutgers.edu).

⊗ Abstract published in *Advance ACS Abstracts,* February 1, 1995.

[1] Abbreviations: BPTI, bovine pancreatic trypsin inhibitor; EGF, epidermal growth factor; mEGF, murine EGF; hEGF, human EGF; TGFα, type-α transforming growth factor; hTGFα, human TGFα; TGFβ, type-β transforming growth factor; CPMG, Carr−Purcell−Meiboom−Gill multipulse sequence; CSA, chemical shift anisotropy; FID, free induction decay; GARP, multipulse nuclear decoupling scheme; NOE, nuclear Overhauser effect; HNOE, heteronuclear NOE; PFG, pulsed-field gradient; PFG-HNOE, pulsed-field gradient HNOE; rmsd, average local root-mean-squared deviations of atomic positions between pairs of optimally superimposed structures; R_1, longitudinal relaxation rate constant; R_2, transverse relaxation rate constant; SSE, sequence-specific standard error between observed and calculated relaxation parameters; T_1, longitudinal relaxation time constant; T_2, transverse relaxation time constant; TPPI, time-proportional phase incrementation.

0006-2960/95/0434-2408$09.00/0

backbone structures similar to that first described for mEGF (Montelione et al., 1986), with an antiparallel β-sheet in the N-terminal two-thirds of the molecule (i.e., the N-terminal subdomain) and a small "double-hairpin" structure in the C-terminal third of the molecule (i.e., the C-terminal subdomain). Over 300 EGF-like sequences have been identified as domains of larger proteins (Campbell & Bork, 1993), and many of these probably have chain folds similar to those of EGF and TGFα.

The structure of hTGFα (Kline et al., 1990; Harvey et al., 1991; Moy et al., 1993) at pH 6.5 consists of two overlapping subdomains: the N-terminal subdomain (residues Val-1−His-35) containing the A (Cys-8−Cys-21) and B (Cys-16−Cys-32) disulfide loops and the C-terminal subdomain (residues Cys-34−Ala-50) containing the C (Cys-34−Cys-43) disulfide loop. Both subdomains contain side-chain residues that appear to be involved in receptor recognition (Campbell & Bork, 1993).

While the three-dimensional structures of hTGFα and other EGF-like proteins have been studied extensively, relatively little is known about conformational dynamics of these molecules. At pH 3.5, all of the hydrogen-bonded amide protons of hTGFα exhibit $^1H/^2H$ exchange half-lives of <1 h (Brown et al., 1989; Montelione et al., 1989), while under identical conditions of pH and temperature many of the corresponding amide protons of mEGF have $^1H/^2H$ exchange half-lives of many weeks (Montelione et al., 1987, 1988). These differences in amide proton exchange rates have been attributed to partial unfolding of hTGFα at low pH, which accompanies titration of salt-bridge-stabilized hydrogen bonds between residue His-18 in the N-terminal subdomain and residue His-35 in the C-terminal subdomain (Tappin et al., 1989; Moy et al., 1993).

At neutral pH conditions at which hTGFα is biologically active there are other indications of backbone conformational dynamics. For example, in all of the NMR structures of hTGFα (Kline et al., 1990; Harvey et al., 1991; Moy et al., 1993) atomic positions for polypeptide backbone segments Val-1−Cys-16 and Leu-48−Ala-50 are much more poorly defined than the rest of the polypeptide backbone. In particular, the polypeptide loop of residues Cys-8−Cys-16 is poorly defined in all of these hTGFα NMR structures while it is reasonably well-defined in the corresponding portions of the NMR structures of human and mouse EGF (Cooke et al., 1987; Montelione et al., 1987, 1992; Kohda & Inagaki, 1988, 1992a; Kohda et al., 1988). hTGFα also exhibits broad proton resonance line widths for some backbone residues in polypeptide segments His-12−Phe-15 and Tyr-38−Glu-44 (Moy et al., 1993), which are in close proximity in the three-dimensional structure. In addition, many tertiary NOE's observed between the N- and C-terminal subdomains of mEGF are not observed between the corresponding protons of hTGFα at pH 6.5 (Moy et al., 1993). These features lead to the suggestion that inter-subdomain NOE's in hTGFα are quenched or significantly line broadened by inter-subdomain hinge-bending motions (Moy et al., 1993). Low-frequency hinge-bending motions between subdomains are the dominant normal modes predicted for dynamic fluctuations in mEGF (Ikura & Gō, 1993). Polypeptide segments His-12−Phe-15 and Ala-41−Cys-43 in hTGFα contain several side chains that are essential for biological activity (Defeo-Jones et al., 1988, 1989; Engler et al., 1990; Campbell & Bork, 1993), and such hinge-bending motions would affect the relative positions of atoms in the N- and C-terminal subdomains thought to comprise the binding epitope for the EGF receptor. These dynamics could also contribute an important entropic component to the free energy of binding.

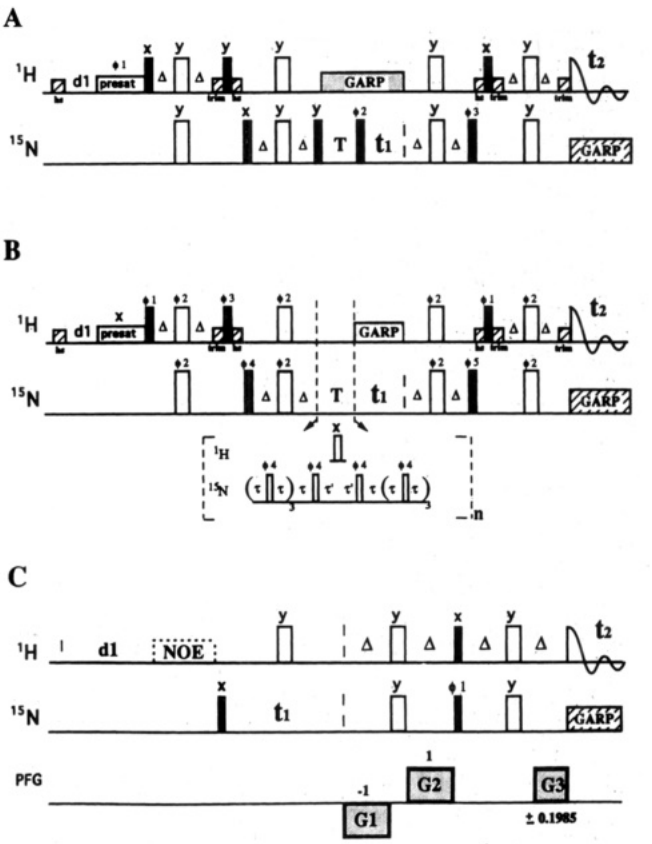

FIGURE 1: Pulse sequence used for measurement of ^{15}N (A) T_1, (B) T_2, and (C) $^1H-^{15}N$ HNOE. The delays Δ are all turned to $^1/_4[^1J(^{15}N-^1H)]$. The phase cycling used for the T_1 experiment was $\phi1 = 4(x), 4(-x), \phi2 = x, -x, \phi3 = 2(y), 2(-y)$, and receiver = $x, -x, -x, x$. For the T_2 experiment, the pulse phases were cycled: $\phi1 = 16(x), 16(y), \phi2 = 16(y), 16(-x), \phi3 = 2(y, y, y, y, -y, -y, -y, -y), 2(-x, -x, -x, -x, x, x, x, x), \phi4 = 8(x, -x), 8(y, -y), \phi5 = 4(x, x, -x, -x), 4(y, y, -y, -y)$, and receiver = $2(-x, x, x, -x, x, -x, -x, x), 2(-y, y, y, -y, y, -y, -y, y)$. For the T_1 and T_2 experiments quadrature detection in ω_1 was achieved by time-proportional phase incremention (Marion & Wüthrich, 1983). Homospoil and trim pulses were used as indicated to improve solvent suppression. The lengths of trim and homospoil pulses were typically 0−4 and 1.5−5 ms, respectively. The phase cycling used for the PFG−HNOE experiment was $\phi1 = y, -y$ and receiver = $x, -x$. Three z-gradient pulses (G1, G2, and G3) are applied during the Δ periods. The ratio of gradient areas G1:G2:G3 was approximately $-1.0:1.0:\pm0.1985$. Quadrature detection in the ω_1 dimension was done by recording two gradient data sets (N- and P-peaks) differing in the phase of final gradient pulse (G3) and then combining these by the method of Nagayama (1986). The PFG amplitudes were 28 G cm^{-1}, and the gradient pulse lengths were 2.6 ms for G1 and G2 and 0.52 ms for G3. Heteronuclear decoupling was carried out during detection using GARP (Shaka et al., 1985) in all three experiments.

In this paper we describe nuclear relaxation measurements which probe the molecular dynamics of hTGFα in aqueous solution at neutral pH. In order to characterize conformational dynamics of hTGFα on both the fast (i.e., sub-nanosecond) and intermediate nitrogen-15 chemical-exchange (ca. microsecond) time scales, we measured nitrogen-15 relaxation parameters at pH 7.1 ± 0.1 and a temperature of 30 ± 0.1 °C. Measurements of nitrogen-15 longitudinal (R_1)

and transverse (R_2) relaxation rates, and $^1H-^{15}N$ heteronuclear NOE effects, were then interpreted using an extended Lipari–Szabo analysis (Lipari & Szabo, 1982a,b; Clore et al., 1990) to provide estimates of the locations and amplitudes of fast internal motions and the locations of nitrogen-15 chemical-exchange line broadening. These results demonstrate that, under conditions of pH and temperature at which it is tightly bound by the EGF receptor, hTGFα is a highly dynamic molecule. Indeed, some 40% of the backbone amide groups of hTGFα, including many at the interface between the two subdomains, exhibit significant nitrogen-15 chemical-exchange line broadening indicative of interconversions between multiple protein conformations on the microsecond time scale.

MATERIALS AND METHODS

NMR Spectroscopy. Samples for NMR spectroscopy were prepared in aqueous solutions containing 2 mM [^{15}N]TGFα protein concentration at pH 7.1 ± 0.1 and 1 mM NaN_3. Samples were prepared by dissolving the protein directly in 90% ^1H_2O/10% ^2H_2O. All NMR experiments were carried out at 30 °C on a Varian Unity 500 spectrometer. Proton and nitrogen-15 resonance assignments for hTGFα at neutral pH have been reported elsewhere (Moy et al., 1993).

Pulse sequences used for measuring the ^{15}N T_1 and T_2 relaxation times and $^1H-^{15}N$ heteronuclear NOE (HNOE) are shown in Figure 1. During the relaxation period T of the T_1 measurement (Figure 1A), proton decoupling with GARP (Shaka et al., 1985) was used to eliminate effects of cross-correlation between dipolar and chemical shift anisotropic (CSA) relaxation mechanisms (Boyd et al., 1990; Stone et al., 1992). In the T_2 measurements, ^{15}N spin-locking was carried out using the Carr–Purcell–Meiboom–Gill (CPMG) spin–echo sequence (Carr & Purcell, 1954; Meiboom & Gill, 1958) during the transverse relaxation period T (Figure 1B). This CPMG spin–echo sequence was modified to minimize cross-correlation effects, as described elsewhere (Kay et al., 1992; Palmer et al., 1992). Proton 180° pulses were applied every 6.2 ms at the peak of the fourth even spin echo of the CPMG sequence in order to invert the ^1H spin state rapidly compared to the fastest decaying component of the ^{15}N doublet. This allowed determination of the average relaxation rate of the two $^{15}N-^1H$ multiplet components. Sample heating was minimized by using a duty cycle of less than 10% during the ^{15}N CPMG sequence. The delay 2τ between successive ^{15}N 180° pulses applied during the CPMG sequence (Figure 1B) was adjusted to 720 μs (τ = 360 μs), and the delay τ' is set so $2\tau' + {}^1H$ 180° pulse width = 2τ. Under these conditions, the value of τ is much less than $1/(2 \times {}^1J_{NH})$, minimizing the contributions of antiphase relaxation pathways to the measured values of T_2.

All T_1, T_2, and HNOE experiments were recorded in duplicate. For T_1 measurements, seven T delays of 50, 100, 200, 300, 500, 700, and 900 ms and nine T delays of 20, 50, 90, 150, 220, 300, 450, 600, and 800 ms for the two data sets, respectively, were used, while for T_2 measurements T delays of 12, 31, 55, 80, 104, 153, and 196 ms and 12, 31, 55, 80, 104, 135, 166, and 196 ms for two data sets, respectively, were used. The total recycle times were 2.3 and 3.3 s for the T_1 and T_2 measurements, respectively.

Heteronuclear $^1H-^{15}N$ NOE's (HNOE's) were measured using the pulsed-field gradient HNOE pulse sequence (Li & Montelione, 1994) shown in Figure 1C. Water suppression was achieved using heteronuclear coherence selection with two gradient pulses (G1 and G2) during the first delay period 2Δ and a final gradient pulse (G3) 100 μs prior to beginning signal detection. A long recycle delay (15 s, approximately $5T_1$ of water) was used to provide complete relaxation of solvent magnetization between each experiment, avoiding saturation-transfer effects which result from partially saturated H_2O magnetization present at the end of the HNOE experiment (Li & Montelione, 1993, 1994). Amide proton saturation (>99%) during the NOE period was achieved using GARP decoupling (Shaka et al., 1985) for 3.7 s, approximately $5T_1$ of the longest backbone amide ^{15}N nucleus (except that of Ala-50), to ensure generation of steady-state HNOE.

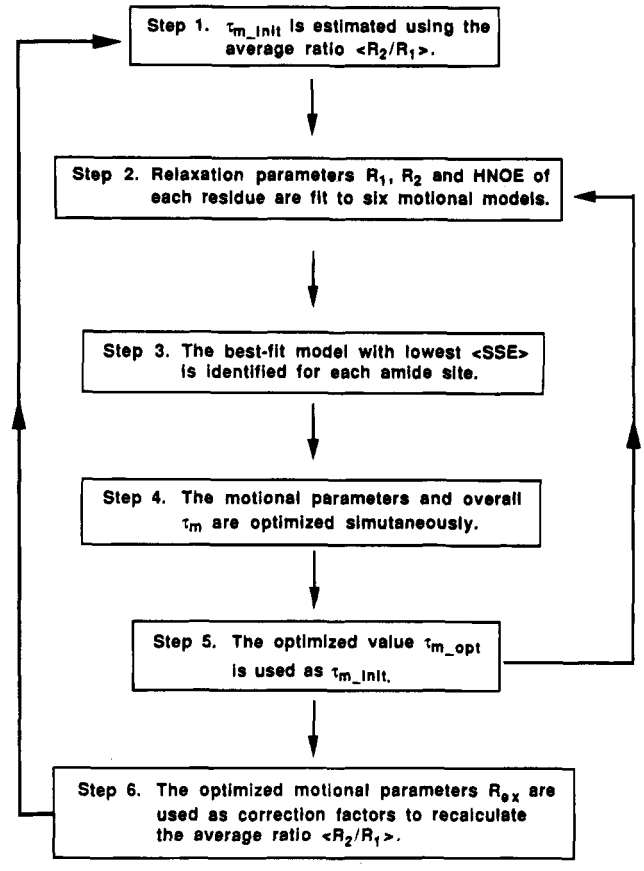

FIGURE 2: Flow chart showing the strategy used for estimating the global value of τ_m and for optimization of extended Lipari–Szabo motional parameters.

All experiments described above were recorded with a sweep width of 3499.6 Hz in the ω_2 dimension with the carrier set to the center of amide proton region of the spectrum. A total of 180 TPPI increments, each of 1024 complex data points, and a sweep width of 3200 Hz in the ω_1 dimension were recorded in the T_1 and T_2 experiments. A total of 90 hypercomplex increments, each of 1024 complex data points, and a sweep width of 3200 Hz in the ω_1 dimension were recorded in PFG-HNOE experiments. Sixty-four transients per t_1 increment were recorded for T_1 and T_2 experiments and 36 transients for the HNOE experiments. No baseline or ridge corrections were required.

Data Analysis

Calculation of T_1, T_2, and HNOE. Relaxation rate constants and HNOE's were calculated from cross-peak

Table 1: Expressions for Spectral Density Functions Used in Analysis of ^{15}N Relaxation Data

model	spectral density functions	optimized parameters
1	$J(\omega) = {}^2/_5[S^2\tau_m/(1+\omega^2\tau_m^2)]$	S^2
2[a]	$J(\omega) = {}^2/_5[S^2\tau_m/(1+\omega^2\tau_m^2) + (1-S^2)\tau_e'/(1+\omega^2\tau_e'^2)]$	S^2, τ_e
3	$J(\omega) = {}^2/_5[S^2\tau_m/(1+\omega^2\tau_m^2)]$ $1/T_{2(obs)} = 1/T_2 + R_{ex}$	S^2, R_{ex}
4	$J(\omega) = {}^2/_5[S^2\tau_m/(1+\omega^2\tau_m^2) + (1-S^2)\tau_e'/(1+\omega^2\tau_e'^2)]$ $1/T_{2(obs)} = 1/T_2 + R_{ex}$	S^2, τ_e, R_{ex}
5[b]	$J(\omega) = {}^2/_5[S^2\tau_m/(1+\omega^2\tau_m^2) + S_f^2(1-S_s^2)\tau_s'/(1+\omega^2\tau_s'^2)]$	S_f^2, S_s^2, τ_e
6	$J(\omega) = {}^2/_5[S^2\tau_m/(1+\omega^2\tau_m^2) + S_f^2(1-S_s^2)\tau_s'/(1+\omega^2\tau_s'^2)]$ $1/T_{2(obs)} = 1/T_2 + R_{ex}$	S_f^2, S_s^2, τ_s, R_{ex}

[a] $\tau_e' = \tau_m\tau_e/(\tau_m + \tau_e)$. [b] $\tau_s' = \tau_m\tau_s/(\tau_m + \tau_s)$; $S^2 = S_f^2S_s^2$.

heights in the $^1H-^{15}N$ correlation spectra. The longitudinal relaxation times, T_1, were obtained by a three-parameter (I_∞, I_0, and T_1) nonlinear least squares fit of eq 1 to the experimental data.

$$I(t) = I_\infty - (I_\infty - I_0)\exp(-t/T_1) \quad (1)$$

The transverse relaxation times, T_2, were obtained by a two-parameter (I_0 and T_2) nonlinear least squares fit of eq 2 to the experimental data.

$$I(t) = I_0\exp(-t/T_2) \quad (2)$$

where I_0 and I_∞ are the initial and final cross-peak heights, respectively. Curve fitting was done using the Levenburg–Marquardt algorithm (Press et al., 1986) in SigmaPlot Scientific Graphing System software (Jandel Corp.). Steady-state $^1H-^{15}N$ HNOE's were calculated from two data sets

$$\text{HNOE} = I_{sat}/I_{eq} \quad (3)$$

in which I_{sat} and I_{eq} are the peak intensities in the spectra recorded with and without saturation of protons during the NOE delay period. The relaxation rate constants, $R_1 = 1/T_1$, $R_2 = 1/T_2$, and HNOE values for order parameter calculations were taken from the mean values of the fitting results of two independent measurements.

Calculation of Extended Lipari–Szabo Motional Parameters. For a two-spin $^{15}N-^1H$ system, the relaxation rates, R_1, R_2, and steady-state HNOE can be expressed as (Abragam, 1961; Becker, 1972)

$$R_1 = (d_{NH}^2/4)[J(\omega_H - \omega_N) + 3J(\omega_N) + 6J(\omega_H + \omega_N)] + (\omega_N^2/3)(\sigma_{||} - \sigma_\perp)^2J(\omega_N) \quad (4)$$

$$R_2 = (d_{NH}^2/8)[4J(0) + J(\omega_H - \omega_N) + 3J(\omega_N) + 6J(\omega_H) + 6J(\omega_H + \omega_N)] + (\omega_N^2/18)(\sigma_{||} - \sigma_\perp)^2[4J(0) + 3J(\omega_N)] + R_{ex} \quad (5)$$

and

$$\text{HNOE} = 1 + (d_{NH}^2/4R_1)(\gamma_H/\gamma_N)[6J(\omega_H + \omega_N) - J(\omega_H - \omega_N)] \quad (6)$$

which includes both dipolar and chemical shift anisotropic (CSA) relaxation mechanisms. The rate R_{ex} is the additional contribution to R_2 due to slow conformational exchange, and

$$d_{NH} = (h\mu_0\gamma_H\gamma_N/8\pi^2)\langle r_{NH}^{-3}\rangle \quad (7)$$

where h is Plank's constant, γ_H and γ_N are the gyromagnetic ratios of ^1H and ^{15}N, ω_H and ω_N are the Larmor frequencies of ^1H and ^{15}N, respectively, and μ_0 is the permeability of free space. The value r_{NH} is the N–H bond length (0.102 nm), and $\sigma_{||}$ and $\sigma_\perp$ are the parallel and perpendicular components of the ^{15}N chemical shift tensor [$\sigma_{||} - \sigma_\perp = -160$ ppm; (Hiyama et al., 1988)]. The $J(\omega)$'s are spectral density functions which depend on overall tumbling of the macromolecule and on the internal motions of the $^1H-^{15}N$ bond vector.

The three principal components of the inertia tensor have been calculated from the solution structure of hTGFα (Moy et al., 1993) to be in a ratio of 1.37:1.15:1.00. Accordingly, the structure of hTGFα can be modeled as a prolate ellipsoid, with an axial ratio of 1.37:1.00, defined as the ratio of the long to the short semiaxes of the ellipsoid. Relative rotational correlation times for reorientation about these axes were determined using standard expressions (Cantor & Schimmel, 1980). Values of $\tau_a/\tau_{sphere} = 1.13$ and $\tau_b/\tau_{sphere} = 0.99$ were calculated for these two rotational correlation times, relative to that of a sphere of equal volume, for reorientation about the short and long semiaxes, respectively. These calculations demonstrate that the hydrodynamic properties of hTGFα are reasonably approximated by models which assume isotropic tumbling. For isotropic overall reorientation of $^{15}N-^1H$ vectors, the spectral density functions can be represented using the formulation of Lipari and Szabo (Lipari & Szabo, 1982a,b)

$$J(\omega) = (2/5)[S^2\tau_m/(1+\omega^2\tau_m^2) + (1-S^2)\tau_e'/(1+\omega^2\tau_e'^2)] \quad (8)$$

where S^2 is the generalized order parameter. The value τ_m is the overall isotropic rotational correlation time of the molecule, and $\tau_e' = \tau_m\tau_e/(\tau_m + \tau_e)$, where τ_e is a single effective correlation time describing the internal motion. This spectral density function can be simplified to eq 9 if the τ_e is extremely small (i.e., <10 ps).

$$J(\omega) = (2/5)[S^2\tau_m/(1+\omega^2\tau_m^2)] \quad (9)$$

For bond vectors with more complex internal dynamics, the Lipari–Szabo formalism can be empirically extended (Clore et al., 1990a) to include two different time constants for internal motions.

$$J(\omega) = (2/5)[S^2\tau_m/(1+\omega^2\tau_m^2) + (S_f^2 - S^2)\tau_s'/(1+\omega^2\tau_s'^2)] \quad (10)$$

in which $S^2 = S_f^2S_s^2$, S_f^2 is the generalized order parameter for faster motion, and S_s^2 is the generalized order parameter describing the slower motion. In eq 10, $\tau_s' = \tau_s\tau_m/(\tau_m + \tau_s)$, τ_s is the effective internal correlation time describing internal motions on the slower of the two time scales, and the fast internal motion, τ_f, is assumed to be very small (i.e., <10 ps).

Strategy for Optimization of Extended Lipari–Szabo Motional Parameters. As the analysis of nitrogen-15 relaxation data for hTGFα is complicated by significant

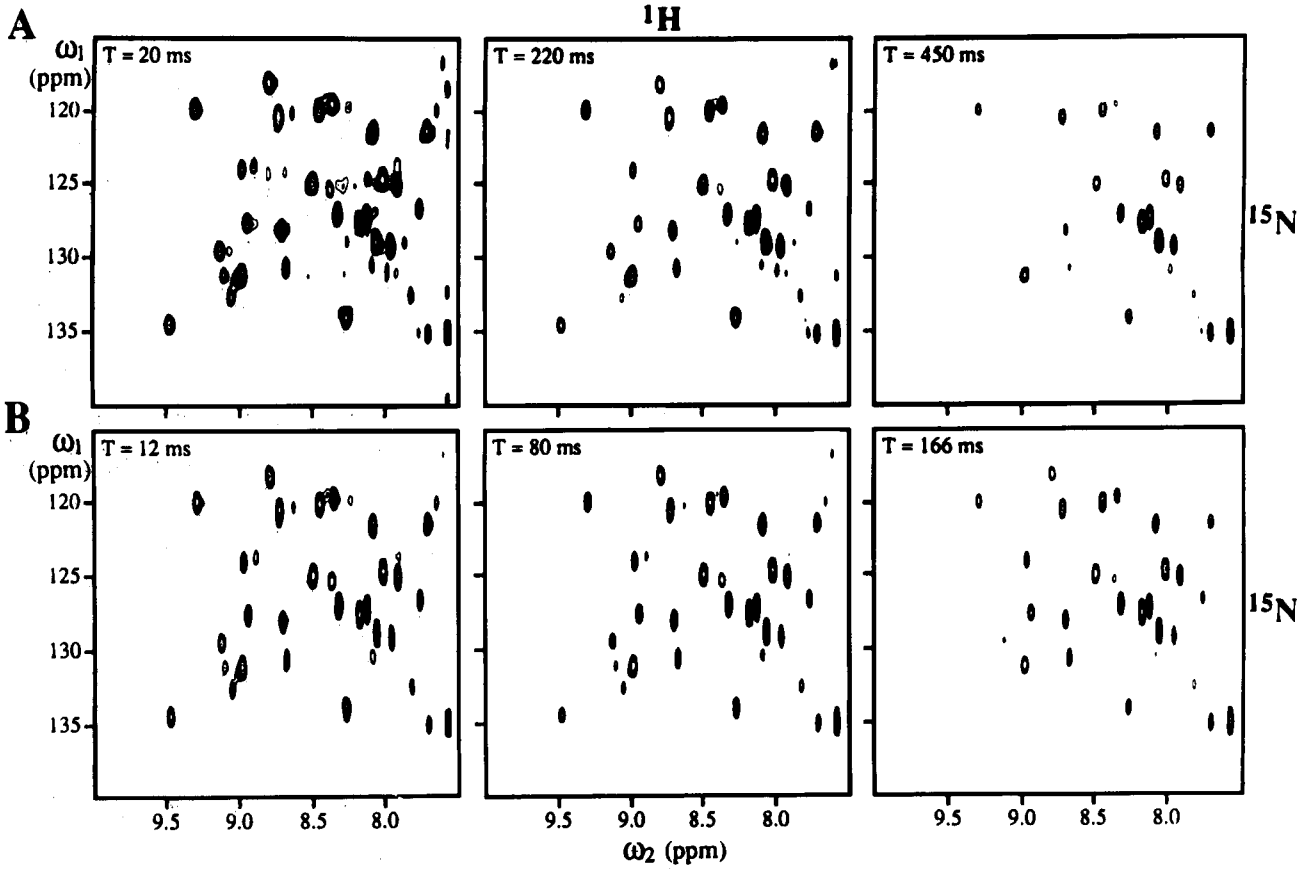

FIGURE 3: Contour plots of a small region of the ^{1}H−^{15}N correlation spectra of hTGFα at pH 7.1 and 30 °C obtained for the ^{15}N T_1 (A) and T_2 (B) experiments at different interval times, T.

contributions from chemical-exchange line broadening, the following strategy (outlined in Figure 2) was used for calculations of order parameters and internal correlation times:

Step 1. An initial value of the overall rotational correlation time, τ_{m_init}, was calculated from the ratio $\langle R_2/R_1 \rangle$, as explained below in the Results section.

Step 2. For each ^{15}N−^{1}H spin system, the relaxation rates R_1, R_2, and HNOE were fit to each of the six models shown in Table 1. The overall rotational correlation time was kept fixed at τ_{m_init}, and optimized order parameters and internal correlation times were obtained by minimization of the following target function (Palmer et al., 1991; Stone et al., 1992)

$$\mathrm{SSE} = (R_1 - R_1^*)^2/\sigma_1^2 + (R_2 - R_2^*)^2/\sigma_2^2 + (\mathrm{HNOE} - \mathrm{HNOE}^*)^2/\sigma_{\mathrm{HNOE}}^2 \quad (11)$$

in which R_1, R_2, and HNOE are the experimental values of relaxation parameters, σ_1, σ_2, and σ_{HNOE} are the uncertainties in these relaxation parameters, and R_1^*, R_2^*, and HNOE* are the corresponding theoretical values computed for each of the six models outlined in Table 1.

Step 3. For each residue a "best-fit" model having the minimum value of the target function (eq 11) was selected. When the results of several models (Table 1) were similar, the simpler one was chosen over any more complex models. The criteria for these selections were based on the values of S_f^2 in models 5 and 6 and R_{ex} in models 4 and 6. When the value of S_f^2 in a model using two internal motions was larger than 0.95 unit, simpler model 2 or 4 was selected rather than complex model 5 or 6, respectively. Similarly, where the optimized value of R_{ex} was less than 0.1 Hz in models 4 or 6, the corresponding simpler models 2 and 5, respectively, were selected instead.

Step 4. Once a model of internal motion which best fit the data was determined for each ^{15}N−^{1}H spin system, the global value of τ_m and internal dynamic parameters of all residues were optimized simultaneously. The global value of τ_m was optimized using the constraints $0 \leq S^2 \leq 1$, $0 \leq \tau_e \leq \tau_m$, and $0 \leq R_{ex}$ and a quadratic interpolation routine (Press et al., 1986) while S^2, τ_e, and R_{ex} were optimized for each residue using the Levenburg−Marquardt algorithm (Press et al., 1986). The resulting value of τ_m was then defined as τ_{m_opt}.

Step 5. The entire process (steps 2−4) was repeated using this final value of τ_{m_opt} as the initial value τ_{m_init}.

Step 6. This analysis allowed identification of ^{15}N−^{1}H sites with significant contributions of chemical-exchange line broadening to the T_2 line width. These sites were then excluded from a recalculation of the $\langle R_2/R_1 \rangle$ ratio (as explained in the Results section), and the entire process (steps 1−5) was repeated.

Error Analysis

Uncertainties in Estimates of R_1, R_2, and HNOE. Uncertainties in estimates of relaxation rates and HNOE values were determined by

$$\sigma = [(R_a - R_{\mathrm{mean}})^2 + (R_b - R_{\mathrm{mean}})^2]^{1/2} \quad (12)$$

where σ is the uncertainty in the relaxation parameters, R_a

and R_b are the two independently measured experimental values, and R_{mean} is the mean value of R_a and R_b. The mean values and uncertainties, σ, of relaxation parameters were used as input in the dynamic analysis (eq 11) and in error estimates described below.

Uncertainties in Extended Lipari−Szabo Parameters. Uncertainties in the best-fit values of motional parameters (S^2, S_f^2, S_s^2, τ_e, and R_{ex}) were estimated by Monte Carlo simulations, using methods developed by Palmer and coworkers (Palmer et al., 1991). In short, values R_1^{bc}, R_2^{bc}, and HNOE^{bc} were back-calculated from the best-fit values of S^2, S_f^2, S_s^2, τ_e, and R_{ex}. Gaussian distributions of $R_1^{err-est}$, $R_2^{err-est}$, and HNOE$^{err-est}$ values were then generated with mean values corresponding to R_1^{bc}, R_2^{bc}, and HNOE^{bc}, respectively, and standard deviations corresponding to the estimated uncertainties in experimental values (i.e., the σ's from eq 12). Five hundred sets of $R_1^{err-est}$, $R_2^{err-est}$, and HNOE$^{err-est}$ were then generated randomly from these distributions and used to compute 500 sets of extended Lipari−Szabo motional parameters. The resulting distributions of motional parameters were considered to provide good estimates of uncertainty if the biases of the motional parameter S^2, τ_e, and R_{ex} were within 15%, 30%, and 10%, respectively, of the corresponding best-fit value. For each motional parameter, the bias is defined as the average difference between the best-fit value and the mean of the simulated distribution, divided by the best-fit value. For complex motional models (models 5 and 6 in Table 1), values S^2 are computed as the product (Clore et al., 1990a,b)

$$S^2 = S_f^2 S_s^2 \quad (13)$$

and standard error estimates σ_r on S^2 were determined by error propagation (Harris & Kratochvil, 1981)

$$\sigma_r = [(\sigma_{rf}/S_f^2) + (\sigma_{rs}/S_s^2)]S^2 \quad (14)$$

where σ_{rf} and σ_{rs} are standard deviations in S_f^2 and S_s^2, respectively, obtained from the simulations described above.

RESULTS

^{15}N T_1, T_2, and HNOE Relaxation Data. Complete quantitative data were obtained for 36 out of a total of 47 (i.e., 77%) backbone secondary amides. For most residues, the nitrogen-15 T_1 and T_2 values lie in the ranges 350−550 ms and 110−200 ms (1.6−2.9 Hz), respectively. The remaining 11 backbone amides did not yield quantitative data either because of insufficient signal-to-noise ratios or partial overlap between two or more peaks in the $^{15}N-^1H$ fingerprint region (Moy et al., 1993), or because their nitrogen-15 assignments have not been determined unambiguously (Moy et al., 1993). A set of three spectra from each of the ^{15}N T_1 and T_2 data sets are shown in Figure 3. Representative data showing decays of cross-peak intensities for several resonances in T_1 and T_2 measurements are plotted against time in Figure 4 and fitted by a three-parameter exponential decay (eq 1) and two parameter exponential decay (eq 2), respectively.

Standard deviations of the R_1 and R_2 rate parameters were obtained from two independent measurements using eq 12. These standard deviations were used in eq 11 as uncertainties in the order parameter calculations. Most of the standard deviations in R_1 and R_2 estimates are less than 10% (Table 2).

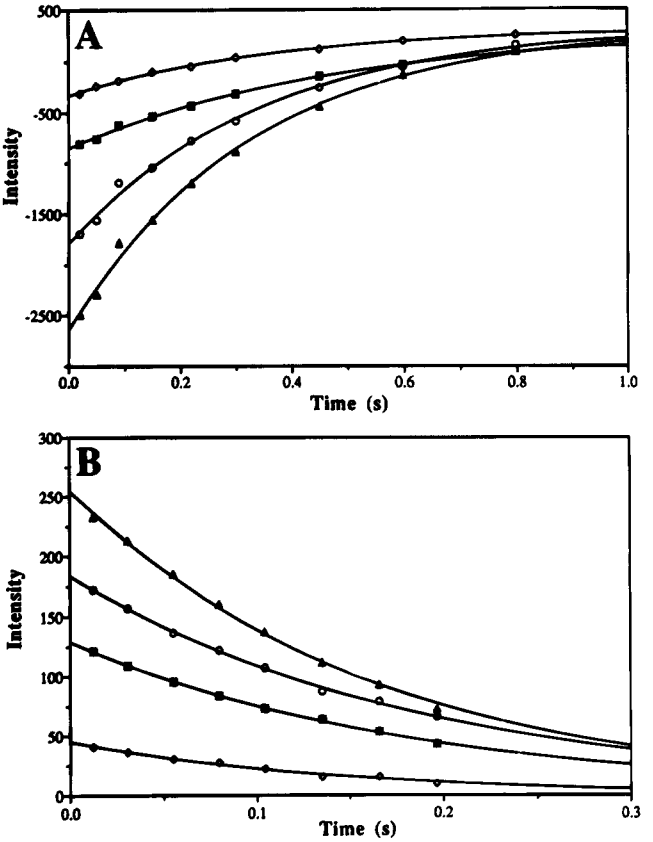

FIGURE 4: T_1 relaxation curves (A) and T_2 relaxation curves (B) for Cys-8 (■), Thr-13 (◇), His-35 (○), and Cys-43 (▲). The T_1 and T_2 curves were obtained by fitting cross-peak intensities recorded in the T_1 and T_2 experiment to eqs 1 and 2, respectively.

The $^1H-^{15}N$ PFG-HNOE experiments were collected with and without 3.7 s of amide proton saturation with GARP. For most residues the measured values of HNOE's are in the range 0.44−0.66 unit. The cross peaks of Leu-48, Leu-49, and Ala-50 have negative intensities in the PFG-HNOE spectrum when the remaining peaks are plotted with positive intensities. As the HNOE experiments were recorded using PFGs and long recycle delays to avoid saturation-transfer effects (Li & Montelione, 1994), it was possible to measure steady-state $^1H-^{15}N$ HNOE's for 41 residues using eq 3. Standard deviations for 80% of the HNOE measurements were smaller than 5%. Only residue His-12 has a uncertainty larger than 10% (Table 2). These ^{15}N R_1, R_2, and HNOE values are tabulated in Table 2 and plotted as a function of residue number in Figure 5.

Estimates of Initial Value of τ_m. The initial value of the overall rotational correlation time, τ_m, was calculated from the mean ratio $\langle R_2/R_1 \rangle$. Assuming a small value of τ_e (i.e., <100 ps), the R_2/R_1 ratio is essentially independent of S^2 and can be used to determine the overall rotational correlation time, τ_m, directly (Kay et al., 1989). However, this approximation also assumes negligible contributions from chemical-exchange line broadening to the measured R_2 values. As will be demonstrated below, in hTGFα many backbone nitrogen-15 nuclei exhibit significant line broadening due to chemical exchange on the microsecond time scale between multiple conformational states. In order to overcome this complication, three different approaches were used for making initial estimates of τ_m. In cycle A, we excluded from the calculation of ratios $\langle R_2/R_1 \rangle$ nine residues (i.e., Asp-7, Cys-21, Arg-22, Phe-23, Leu-24, Val-39, Leu-48,

Table 2: ^{15}N Relaxation Parameters for hTGFα at pH 7.1 and 30 °C

residue	R_1 (s^{-1})	R_2 (s^{-1})	HNOE[a]	R_2/R_1	R_{2corr}/R_1[b]
Phe-5			0.28 ± 0.01		
Asn-6	2.61 ± 0.71	5.53 ± 0.58	0.44 ± 0.03	2.12 ± 0.62	2.12 ± 0.62
Asp-7	1.96 ± 0.17	6.22 ± 0.75	0.46 ± 0.02	3.18 ± 0.48	2.21 ± 0.43
Cys-8	2.13 ± 0.01	5.70 ± 0.52	0.60 ± 0.01	2.68 ± 0.25	2.26 ± 0.25
Asp-10			0.59 ± 0.03		
Ser-11			0.59 ± 0.01		
His-12			0.46 ± 0.11		
Thr-13	2.69 ± 0.08	7.04 ± 0.21	0.58 ± 0.03	2.62 ± 0.11	2.25 ± 0.11
Phe-15	2.84 ± 0.43	7.73 ± 0.49	0.62 ± 0.01	2.72 ± 0.44	2.58 ± 0.42
Cys-16	2.78 ± 0.27	8.15 ± 0.79	0.62 ± 0.01	2.93 ± 0.40	2.26 ± 0.36
Phe-17	2.53 ± 0.23	6.26 ± 0.52	0.56 ± 0.01	2.47 ± 0.30	2.12 ± 0.28
His-18	2.32 ± 0.30	6.09 ± 0.40	0.53 ± 0.05	2.63 ± 0.38	2.23 ± 0.33
Gly-19	2.81 ± 0.09	5.95 ± 0.51	0.62 ± 0.01	2.12 ± 0.19	2.12 ± 0.19
Thr-20	2.71 ± 0.18	6.32 ± 0.56	0.63 ± 0.01	2.33 ± 0.26	2.26 ± 0.25
Cys-21	2.99 ± 0.87	9.46 ± 0.61	0.61 ± 0.04	3.16 ± 0.94	2.13 ± 0.65
Arg-22	2.85 ± 0.16	10.95 ± 0.73	0.64 ± 0.01	3.85 ± 0.34	2.24 ± 0.29
Phe-23	2.62 ± 0.10	8.44 ± 0.62	0.58 ± 0.01	3.22 ± 0.27	2.25 ± 0.25
Leu-24	2.72 ± 0.21	8.93 ± 0.65	0.53 ± 0.03	3.29 ± 0.35	2.23 ± 0.30
Val-25	2.87 ± 0.37	8.65 ± 0.47	0.49 ± 0.01	3.01 ± 0.42	1.96 ± 0.30
Gln-26	2.75 ± 0.13	6.82 ± 1.46	0.51 ± 0.03	2.48 ± 0.55	2.15 ± 0.54
Glu-27	2.66 ± 0.40	6.78 ± 0.33	0.46 ± 0.02	2.55 ± 0.41	2.18 ± 0.35
Asp-28	2.64 ± 0.38	5.92 ± 0.50	0.51 ± 0.01	2.24 ± 0.37	2.22 ± 0.37
Lys-29	2.78 ± 0.15	8.27 ± 0.36	0.50 ± 0.01	2.98 ± 0.21	2.05 ± 0.17
Ala-31	2.50 ± 0.22	5.36 ± 0.29	0.62 ± 0.01	2.14 ± 0.22	2.14 ± 0.22
Cys-32	2.66 ± 0.26	7.40 ± 0.57	0.61 ± 0.02	2.78 ± 0.35	2.26 ± 0.31
Val-33	2.96 ± 0.29	8.28 ± 0.69	0.61 ± 0.03	2.80 ± 0.36	1.93 ± 0.30
Cys-34	2.86 ± 0.11	6.06 ± 1.19	0.63 ± 0.05	2.12 ± 0.43	2.12 ± 0.43
His-35	2.85 ± 0.05	5.49 ± 0.46	0.61 ± 0.01	1.92 ± 0.16	1.92 ± 0.16
Ser-36	2.92 ± 0.61	6.21 ± 0.74	0.63 ± 0.02	2.13 ± 0.51	2.09 ± 0.51
Tyr-38	2.83 ± 0.23	5.85 ± 0.59	0.63 ± 0.01	2.07 ± 0.27	2.07 ± 0.27
Val-39	2.51 ± 0.01	8.96 ± 0.81	0.63 ± 0.01	3.58 ± 0.32	2.26 ± 0.32
Gly-40	2.53 ± 0.12	6.98 ± 0.40	0.60 ± 0.02	2.76 ± 0.21	2.25 ± 0.19
Ala-41			0.65 ± 0.03		
Cys-43	2.98 ± 0.12	6.33 ± 0.44	0.62 ± 0.01	2.12 ± 0.17	1.91 ± 0.17
Glu-44	3.18 ± 0.19	6.73 ± 0.68	0.67 ± 0.01	2.12 ± 0.25	2.07 ± 0.25
His-45	2.89 ± 0.29	6.86 ± 0.50	0.61 ± 0.01	2.38 ± 0.29	2.19 ± 0.28
Ala-46	2.68 ± 0.06	5.19 ± 0.62	0.60 ± 0.02	1.94 ± 0.23	1.94 ± 0.23
Asp-47	2.49 ± 0.02	5.37 ± 0.48	0.48 ± 0.01	2.16 ± 0.19	2.08 ± 0.19
Leu-48	1.94 ± 0.24	3.37 ± 0.46	−0.19 ± 0.01	1.73 ± 0.32	1.73 ± 0.32
Leu-49	1.77 ± 0.36	2.56 ± 0.42	−0.48 ± 0.01	1.45 ± 0.37	1.45 ± 0.37
Ala-50	1.18 ± 0.22	1.35 ± 0.36	−1.12 ± 0.02	1.15 ± 0.38	1.15 ± 0.38

[a] Where error bars smaller than ±0.01 were observed, the error is reported as ±0.01. The error bars represent the standard devivation (σ) computed using eq 12. [b] $R_{2corr} = R_2 - R_{ex}$.

Leu-49, and Ala-50) that have ratios $\langle R_2/R_1 \rangle$ outside one standard deviation (±0.58 unit) of the mean value. One of these residues (i.e., Asp-7) has an unusually high T_1 value, and five of the nine residues have very small T_2 values (i.e., Cys-21, Arg-22, Phe-23, Leu-24, and Val-39) which appear to be affected by nitrogen-15 chemical-exchange line broadening (Table 2). Three residues (Leu-48, Leu-49, and Ala-50) located at the C-terminus of the protein exhibit high mobility on the sub-nanosecond time scale (see Figure 5) and were also excluded in the initial τ_m estimate. The average ratio $\langle R_2/R_1 \rangle$ for the remaining 27 residues was then used to estimate an initial value of $\tau_{m\_init} = 4.39 \pm 0.05$ ns.

In cycle B, a total of 13 residues were excluded from the estimate of τ_{m_init} from R_2/R_1 ratios. In addition to the nine residues excluded in the cycle A analysis, residues Cys-16, Val-25, Lys-29, and Val-33 having best-fit values of $R_{ex} >$ 1.5 Hz (Table 2, cycle A) were also excluded in calculating the $\langle R_2/R_1 \rangle$ ratio. The average ratios $\langle R_2/R_1 \rangle$ for the remaining 23 residues were then used to estimate $\tau_{m\_init} = 4.25 \pm 0.05$ ns. Once again, the best of six motional models (Table 1) was identified for each residue, and then τ_m was optimized simultaneously with the model-free parameters (Figure 2).

In both cycles A and B, the value τ_{m_opt} was smaller than the initial estimate τ_{m_init}. This is because many amide protons in hTGFα have significant contributions to R_2 from chemical-exchange line broadening (Table 3), resulting in overestimates of τ_{m_init} from R_2/R_1 ratios. We attempted to better correct for these errors in estimating τ_{m_init} in cycle C. For the amide groups of hTGFα which exhibit nitrogen-15 chemical-exchange linebroadening in cycle B, the value $R_{2corr} = R_2 - R_{ex}$ was computed, using the R_{ex} parameter obtained in cycle B. Having made this correction, the mean ratio $\langle R_2/R_1 \rangle$ was determined by excluding nine sites with R_{2corr}/R_1 ratios outside one standard deviation of the mean value (Table 4) and used to estimate $\tau_{m\_init} = 3.96 \pm 0.05$ ns. Steps 2−5 of Figure 2 were then repeated, optimizing first the motional model (Table 1) and parameters with fixed overall rotational correlation time and then simultaneously optimizing the motional parameters and overall correlation time for the best model.

Values of τ_{m_init} and τ_{m_opt} and values of the target function (eq 11) summed over all residues (ΣSSE) at the end of cycles A, B, and C are presented in Table 4. The optimized value of the summed target function ΣSSE became smaller as improved estimates of τ_{m_opt} were made. For hTGFα at pH 7.1 and a temperature of 30 °C, the minimum value of the target function was obtained for an overall rotational correlation time τ_m of 3.76 ns. Larger values of the summed

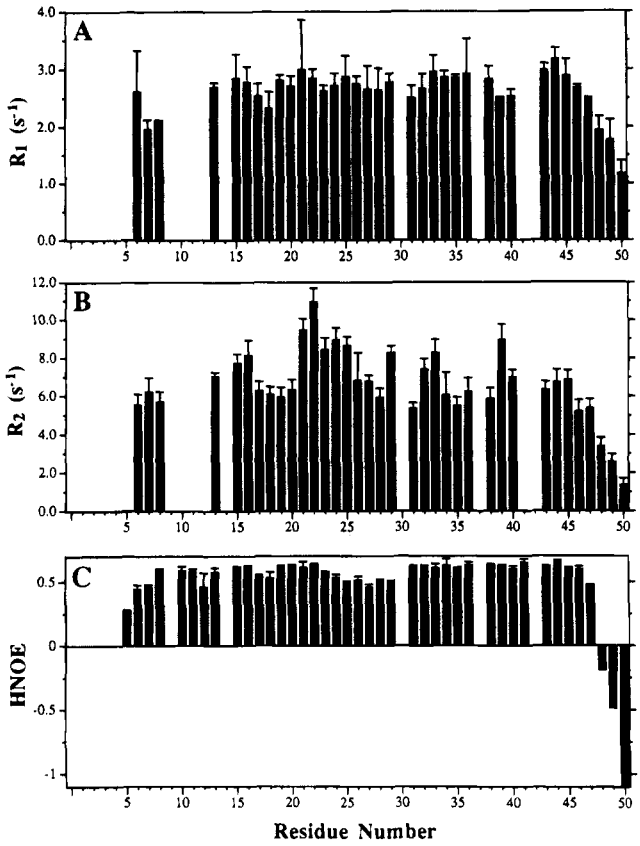

FIGURE 5: (A) R_1, (B) R_2, and (C) HNOE values for hTGFα measured at pH 7.1 and a temperature of 30 °C using a 500-MHz NMR spectrometer, plotted as a function of residue number. R_1, R_2, and HNOE values are the average of the two data sets. The uncertainties shown represent the range of values obtained in the two measurements.

target function ΣSSE were obtained using values of τ_m <3.7 ns.

Optimization of Extended Lipari−Szabo Motional Parameters. Optimized values of motional parameters for hTGFα at pH 7.1 and 30 °C at the ends of each of the three cycles described above are summarized in Table 3. For 29 amide sites, the best-fit models were the same at the end of each cycle and independent of the initial estimate of τ_m. However, for the remaining seven sites it was found that as the initial choice of τ_m improved, the optimum motional model changed. Generally, converging on τ_m by reiterate analysis results in more simplified descriptions of the internal motion. For example, residue Ala-46 fits best to a multiexponential relaxation process (i.e., model 5) when τ_m was estimated by the procedure of cycles A and B, while the same data fit best to a single-exponential model (i.e., model 2) when τ_m was reiteratively optimized in cycle C. Similar results were obtained for other amide sites (e.g., Ala-31, Cys-32, Ala-46, and Leu-48). On the other hand, residues Asp-28 and Ser-36 fit best to a more complex single-exponential model with chemical-exchange line broadening (model 4) once τ_m was optimally determined. The best-fit order parameter S^2 was also generally independent of the initial τ_m estimate, although the precision of the S^2 estimate generally improved in each cycle. However, for amides of residues Val-25, Ala-46, Asp-47, and Leu-48, the optimized value of S^2 did depend on the initial estimate of τ_m (Table 3).

It is generally easier to fit experimental data to models with more adjustable parameters, and care was taken to avoid overfitting the available data. In these measurements, three experimental relaxation parameters (R_1, R_2, and HNOE) are determined for each residue. Models 1−5 in Table 1 consist of three or fewer adjustable parameters per residue, while model 6 includes four adjustable parameters per residue. For hTGFα at pH 7.1, nearly all of the backbone amide sites for which data are available could be fit using models 1−5. However, for the amide of residue Asp-47, the relaxation data was best fit to a complex motional model with a small amount of chemical-exchange line broadening (i.e., model 6 with $R_{ex} \approx 0.4$ Hz). Considering that only three relaxation parameters were measured for this residue and that the apparant chemical-exchange line broadening is within the uncertainty level, these data were subsequently forced to fit complex model 5 with no chemical-exchange line broadening (i.e., cycle D for Asp-47 in Table 3). The values of S^2 and τ_e obtained from this final fit to model 5 for Asp-47 were almost identical to those obtained for model 6.

Most of the amide sites for which data are available could be fit using simple Lipari−Szabo analysis (eq 8), with or without chemical-exchange line broadening. Of the 36 sites analyzed, only three in the C-terminal tail of hTGFα (i.e., Asp-47, Leu-49, and Ala-50) required fitting to more complex models. For 25 of these sites, optimal fitting required the inclusion of a ^{15}N chemical-exchange line broadening term. The order parameters S^2 and chemical exchange terms R_{ex} for these sites are plotted in Figure 6. Most sites have order parameters in the range 0.8−0.95 unit, with uncertainties generally less than ±0.05 unit.

Distribution of Fast Internal Motions of Backbone Amides in hTGFα. The distribution of amide sites with motional order parameters S^2 in the ranges 0.8−1.0, 0.6−0.8, and <0.6 unit is summarized on the solution NMR structure (Moy et al., 1993) in Figure 7A. Sites exhibiting order parameters indicative of larger amplitude sub-nanosecond motions (S^2 < 0.8 unit) include Asp-7 and Cys-8, located in a bend in the N-terminal polypeptide segment of hTGFα, and Leu-48, Leu-49, and Ala-50 in the C-terminal polypeptide segment. In addition, values of S^2 indicative of internal motions are also observed for the chain reversals at Phe-17−His-18 (S^2 < 0.8 unit), Glu-27−Asp-28 ($S^2 \approx 0.8$ unit; Figure 6A), and Val-39−Gly-40 ($S^2 \approx 0.8$ unit; Figure 6A). Residues Phe-23 and Ala-31, which are opposite one another in the central β-sheet, also exhibit lower than average order parametes (i.e., S^2 < 0.85 unit).

Estimates of Correlation Times for Internal Motions. While the S^2 and R_{ex} parameters could be measured reliably, estimates of τ_e were much less precise, exhibiting values of 20−1400 ps and uncertainties of 20%−100% (Table 3). The precision in estimates of τ_e depended strongly on the values of S^2: for $S^2 \leq 0.8$ unit, the uncertainties in τ_e are generally less than 25%, while for sites with $S^2 > 0.8$ unit the uncertainties were generally larger. Long τ_e values (>500 ps) are generally associated with complex motional models (Stone et al., 1992; Clore et al., 1990b; Powers et al., 1992; Kördel et al., 1992; Akke et al., 1993b), as is observed for residues Leu-49 and Ala-50. In some cases, unusually long τ_e values were observed for simple motional models using methods A or B for estimating τ_m but were fit best to one of the simpler Lipari−Szabo motional models (i.e., models 1−4 in Table 1) with smaller (<500 ps) values of τ_e once τ_m converged in cycle C. However, several sites were fit to the final models with values τ_e as large as 800−1400 ps

Table 3: Lipari–Szabo Motional Parameters for hTGFα at pH 7.1 and 30 °C

residue	model	S^2	S_f^2	S_s^2	τ_e (ps)	R_{ex} (s^{-1})
6 A[a]	2	0.71 ± 0.16			1184 ± −[b]	
6 B[a]	2	0.76 ± 0.16			930 ± −	
6 C[a]	2	0.83 ± 0.06			520 ± 426	
7 A	4	0.62 ± 0.05			58 ± 15	1.89 ± 0.81
7 B	4	0.61 ± 0.05			55 ± 14	2.07 ± 0.82
7 C	4	0.60 ± 0.05			52 ± 13	2.28 ± 0.82
8 A	4	0.69 ± 0.01			36 ± 1	0.90 ± 0.51
8 B	4	0.69 ± 0.01			32 ± 1	1.10 ± 0.52
8 C	4	0.68 ± 0.01			28 ± 1	1.34 ± 0.52
13 A	4	0.87 ± 0.03			158 ± 123	0.99 ± 0.27
13 B	4	0.86 ± 0.03			132 ± 96	1.24 ± 0.27
13 C	4	0.85 ± 0.03			108 ± 67	1.54 ± 0.27
15 A	4	0.91 ± 0.01			171 ± 15	1.44 ± 0.31
15 B	4	0.90 ± 0.01			1046 ± 39	1.55 ± 0.48
15 C	4	0.91 ± 0.01			122 ± 12	1.92 ± 0.30
16 A	4	0.91 ± 0.01			177 ± 50	1.85 ± 0.43
16 B	4	0.90 ± 0.01			135 ± 46	2.11 ± 0.48
16 C	4	0.89 ± 0.01			101 ± 27	2.43 ± 0.52
17 A	2	0.86 ± 0.01			162 ± 18	
17 B	6	0.71 ± 0.06	0.89 ± 0.07	0.80 ± 0.01	1390 ± 96	1.10 ± 0.64
17 C	4	0.80 ± 0.02			84 ± 15	1.10 ± 0.40
18 A	4	0.75 ± 0.06			77 ± 61	0.90 ± 0.54
18 B	4	0.74 ± 0.07			71 ± 77	1.12 ± 0.60
18 C	4	0.73 ± 0.08			64 ± 86	1.38 ± 0.61
19 A	2	0.84 ± 0.09			1801 ± 941	
19 B	2	0.91 ± 0.01			148 ± 41	
19 C	2	0.91 ± 0.01			118 ± 30	
20 A	4	0.89 ± 0.01			115 ± 31	0.18 ± −[b]
20 B	4	0.88 ± 0.02			93 ± 28	0.44 ± 0.36
20 C	4	0.87 ± 0.02			72 ± 20	0.75 ± 0.43
21 A	4	0.91 ± 0.07			718 ± −	3.07 ± 0.58
21 B	4	0.92 ± 0.07			727 ± −	3.25 ± 0.53
21 C	4	0.91 ± 0.06			996 ± −	3.50 ± 0.56
22 A	4	0.91 ± 0.01			1134 ± 116	4.56 ± 0.74
22 B	4	0.91 ± 0.01			1197 ± 118	4.73 ± 0.74
22 C	4	0.92 ± 0.01			1271 ± 132	4.93 ± 0.74
23 A	4	0.85 ± 0.01			122 ± 15	2.54 ± 0.46
23 B	4	0.84 ± 0.01			106 ± 12	2.79 ± 0.48
23 C	4	0.83 ± 0.01			88 ± 11	3.08 ± 0.51
24 A	4	0.83 ± 0.02			945 ± 154	2.92 ± 0.65
24 B	4	0.86 ± 0.02			200 ± 105	3.11 ± 0.46
24 C	4	0.85 ± 0.02			162 ± 97	3.41 ± 0.53
25 A	4	0.65 ± 0.12			1844 ± 636	3.21 ± 0.53
25 B	4	0.74 ± 0.04			1354 ± 254	3.11 ± 0.49
25 C	4	0.85 ± 0.01			626 ± 54	3.03 ± 0.48
26 A	4	0.80 ± 0.23			1061 ± −	0.94 ± 1.07
26 B	4	0.79 ± 0.13			1124 ± 793	1.12 ± −
26 C	4	0.86 ± 0.02			211 ± 167	1.25 ± −
27 A	4	0.76 ± 0.02			1025 ± 102	1.09 ± 0.34
27 B	4	0.79 ± 0.03			846 ± 201	1.15 ± 0.34
27 C	4	0.82 ± 0.01			198 ± 76	1.44 ± 0.34
28 A	2	0.81 ± 0.06			977 ± 367	
28 B	4	0.83 ± 0.01			170 ± 22	0.27 ± −
28 C	4	0.83 ± 0.01			144 ± 19	0.56 ± 0.30
29 A	4	0.66 ± 0.23			1828 ± −	2.78 ± 0.55
29 B	4	0.76 ± 0.03			1278 ± 223	2.68 ± 0.38
29 C	4	0.86 ± 0.01			570 ± 128	2.61 ± 0.28
31 A	5	0.72 ± 0.19	0.87 ± 0.04	0.83 ± 0.18	1866 ± −	
31 B	5	0.79 ± 0.10	0.86 ± 0.03	0.92 ± 0.09	795 ± −	
31 C	2	0.83 ± 0.03			55 ± 15	
32 A	6	0.79 ± 0.14	0.93 ± 0.08	0.85 ± 0.08	1467 ± 902	1.62 ± 0.76
32 B	4	0.86 ± 0.03			93 ± 45	1.63 ± 0.46
32 C	4	0.85 ± 0.03			75 ± 50	1.93 ± 0.50
33 A	4	0.58 ± −[b]			3939 ± −	2.58 ± 0.78
33 B	4	0.67 ± −			3488 ± −	2.57 ± 0.71
33 C	4	0.91 ± 0.06			941 ± −	2.32 ± 0.59

Table 3 (Continued)

residue	model	S^2	S_f^2	S_s^2	τ_e (ps)	R_{ex} (s^{-1})
34 A	2	0.85 ± 0.20			1608 ± −	
34 B	2	0.90 ± 0.17			1050 ± −	
34 C	2	0.92 ± 0.07			135 ± −	
35 A	2	0.76 ± 0.08			2379 ± 694	
35 B	2	0.82 ± 0.06			1899 ± 611	
35 C	2	0.91 ± 0.01			155 ± 32	
36 A	2	0.91 ± 0.01			154 ± 48	
36 B	4	0.90 ± −			1201 ± −	0.01 ± −
36 C	4	0.91 ± 0.30			1330 ± −	0.22 ± −
38 A	2	0.90 ± 0.01			113 ± 22	
38 B	2	0.90 ± 0.01			113 ± 22	
38 C	2	0.91 ± 0.01			108 ± 24	
39 A	4	0.82 ± 0.01			61 ± 5	3.28 ± 0.81
39 B	4	0.81 ± 0.01			53 ± 5	3.53 ± 0.81
39 C	4	0.81 ± 0.01			43 ± 4	3.81 ± 0.81
40 A	4	0.83 ± 0.04			81 ± 52	1.27 ± 0.48
40 B	4	0.82 ± 0.04			71 ± 40	1.51 ± 0.48
40 C	4	0.81 ± 0.04			59 ± 27	1.80 ± 0.48
43 A	4	0.80 ± −			2229 ± −	0.01 ± 0.50
43 B	4	0.91 ± 0.06			935 ± 853	0.13 ± −
43 C	4	0.91 ± 0.04			1093 ± 575	0.36 ± 0.34
44 A	4	0.95 ± 0.01			773 ± 19	0.14 ± 0.45
44 B	4	0.95 ± 0.01			932 ± 30	0.33 ± −
44 C	4	0.96 ± 0.01			121 ± 25	0.64 ± 0.57
45 A	4	0.82 ± 0.06			1799 ± 584	0.75 ± 0.48
45 B	4	0.90 ± 0.01			901 ± 103	0.70 ± 0.47
45 C	4	0.89 ± 0.02			1210 ± 301	0.95 ± 0.49
46 A	5	0.56 ± 0.23	0.91 ± 0.03	0.61 ± 0.23	3488 ± −	
46 B	5	0.63 ± −	0.91 ± 0.03	0.69 ± 0.24	3040 ± −	
46 C	2	0.85 ± 0.02			87 ± 24	
47 A	6	0.64 ± 0.02	0.91 ± 0.01	0.70 ± 0.01	1416 ± 30	0.31 ± −
47 B	6	0.68 ± 0.02	0.90 ± 0.01	0.75 ± 0.01	1168 ± 18	0.37 ± 0.36
47 C	6	0.77 ± 0.02	0.90 ± 0.01	0.85 ± 0.01	303 ± 2	0.37 ± 0.36
47 D	5	0.77 ± 0.02	0.90 ± 0.01	0.85 ± 0.01	295 ± 3	
48 A	5	0.37 ± 0.04	0.85 ± 0.07	0.44 ± 0.01	738 ± 22	
48 B	5	0.39 ± 0.04	0.86 ± 0.07	0.45 ± 0.01	714 ± 21	
48 C	2	0.49 ± 0.01			181 ± 8	
49 A	5	0.16 ± 0.05	0.85 ± 0.10	0.19 ± 0.04	957 ± 74	
49 B	5	0.18 ± 0.06	0.85 ± 0.10	0.21 ± 0.04	933 ± 68	
49 C	5	0.20 ± 0.05	0.84 ± 0.10	0.24 ± 0.03	892 ± 54	
50 A	5	0.01 ± −	0.66 ± 0.10	0.02 ± 0.04	840 ± 93	
50 B	5	0.01 ± −	0.66 ± 0.10	0.02 ± 0.04	844 ± 93	
50 C	5	0.10 ± 0.04	0.61 ± 0.09	0.16 ± 0.04	633 ± 67	

[a] Results are presented for three cycles of reiterative estimates of rotational correlation times, cycles A, B, and C of Table 4. [b] Error bars are not reported when the bias between best-fit and back-calculated values, as defined in the text, was >15%, >30%, and >10% for the motional parameters S^2, τ_e, and R_{ex}, respectively.

(i.e., amides of Cys-21, Arg-22, Val-33, Ser-36, Cys-43, and His-45). Control experiments carried out with the same pulse sequences and analysis procedures with ^{15}N-enriched bovine pancreatic trypsin inhibitor (BPTI) exhibit few τ_e values >50 ps and no τ_e values >170 ps except for two residues in the highly flexible C-terminal polypeptide segment (Li and Montelione, unpublished results). It is possible that some of the amide sites in hTGFα which fit best to simple motional models and large τ_e values actually represent amide protons which have both slow and fast sub-nanosecond motions, with small amplitudes for the slower motional component.

Distribution of Slow Internal Motions of Backbone Amides in hTGFα. Twenty-three backbone amide sites were best fit in cycle C with significant (>0.5 Hz) nitrogen-15 chemical-exchange line broadening (Figure 6B). Uncertainties in these values were generally on the order of ±0.3−0.5 Hz. The distribution of these amide sites in the three-dimensional structure of hTGFα (Moy et al., 1993) is summarized in Figure 7B. Sites exhibiting nitrogen-15 chemical-exchange line broadening greater than 0.5 Hz include amides of polypeptide segments Asp-7−Cys-8, Thr-13−His-18, Thr-20−Lys-29, Cys-32−Val-33, Val-39−Gly-40, and Glu-44−His-45. Control experiments carried out with the same pulse sequences and analysis procedures with a sample of ^{15}N-enriched BPTI revealed relatively little nitrogen-15 chemical-exchange line broadening except in the vicinity of the Cys-14−Cys-38 disulfide bond (Li and Montelione, unpublished results). The extensive chemical-exchange line broadening observed for approximately half of the backbone amides of hTGFα at neutral pH is very unusual and indicates interconversion between multiple protein conformations on the microsecond time scale.

Table 4: $\langle R_2/R_1 \rangle$, Overall Correlation Time (τ_m), and Total Minimium Value of the Target Function, SSE, for hTGFα at pH 7.1 and 30 °C

cycle	$\langle R_2/R_1 \rangle$	τ_{m_init} (ns)	τ_{m_opt} (ns)	ΣSSE
A	2.42[a] ± 0.33	4.39 ± 0.05	4.17 ± 0.05	6.70
B	2.33[b] ± 0.27	4.25 ± 0.05	3.99 ± 0.05	4.60
C	2.18[c] ± 0.07	3.96 ± 0.05	3.76 ± 0.05	3.93

[a] The average $\langle R_2/R_1 \rangle$ is obtained from 27 residues, excluding 9 residues (i.e., D7, C21, R22, F23, L24, V39, L48, L49, and A50) that had R_2/R_1 ratios outside one standard devivation (0.58) of the mean value. [b] In addition to the nine residues omitted in cycle A, another four residues (i.e., C16, V25, K29, and V33, having $R_{ex} > 1.5$ Hz after analysis by method A) are also excluded in the calculation of the mean $\langle R_2/R_1 \rangle$ ratio. [c] In cycle C, R_{2corr} is obtained from back-calculation: $R_{2corr} = R_2 - R_{ex}$, where the R_{ex} parameter was obtained from analysis method B. Having made this correction, $\langle R_2/R_1 \rangle$ is obtained by excluding the nine remaining residues (i.e., F15, V25, V33, H35, C43, A46, L48, L49, and A50) with $\langle R_{2corr}/R_1 \rangle$ ratios outside one standard devivation (0.14) of the mean values.

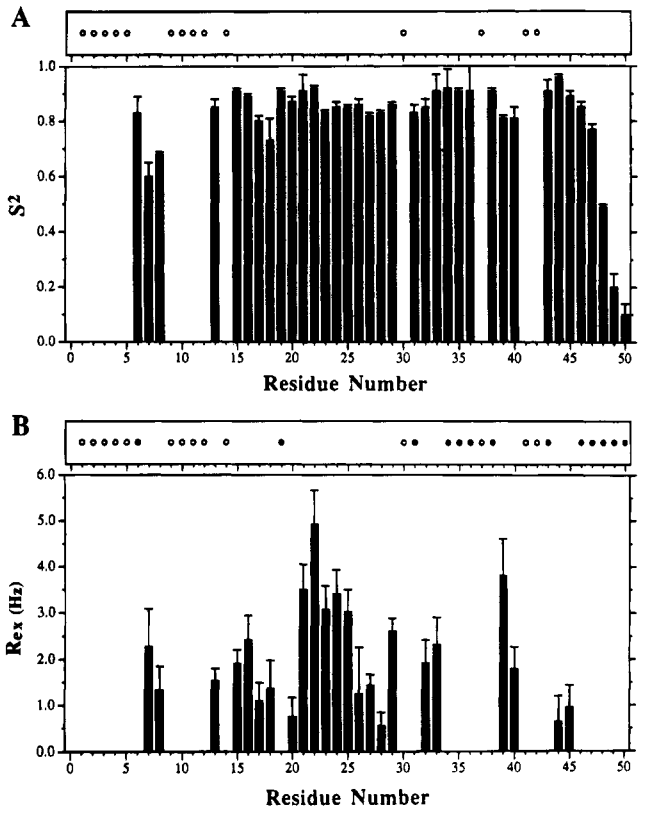

FIGURE 6: Plots as a function of residue number of (A) the Lipari–Szabo order parameter (S^2) and (B) exchange line broadening (R_{ex}) values larger than 0.5 Hz. Data were obtained by fitting the relaxation data at pH 7.1 and 30 °C to models 1–5 and selection of the best fitting model based on minimum values of the target function and criteria described in the text. Amide sites for which reliable estimates of all three dynamic parameters could not be obtained are indicated by open circles in both panels. Sites that were best fit without chemical exchange line broadening (or with $R_{ex} < 0.5$ Hz) are indicated by closed circles.

DISCUSSION

Relaxation Parameters R_1, R_2, and HNOE. The characterization of internal motions from nitrogen-15 relaxation measurements generally involves determination of at least three relaxation parameters per residue, R_1, R_2, and HNOE (Kay et al., 1989). In some cases, additional relaxation parameters may also be determined (Peng & Wagner, 1992). However, it is useful to know if any one or two of these experiments provide useful information for characterizing internal motions. In order to evaluate this, and to provide another view of the distributions of relaxation processes in hTGFα, we compared (Figure 8) three different measures of internal flexibility along the polypeptide sequence: $1 - S^2$, $R_{1\_max} - R_1$, and $HNOE_{max}$ − HNOE, where R_{1_max} and $HNOE_{max}$ were computed from the overall rotational correlation time $\tau_m = 3.76$ ns assuming $S^2 = 1$. Both $R_{1\_max} - R_1$ and $HNOE_{max}$ − HNOE show good correlations with $1 - S^2$, even in polypeptide segments which exhibit significant chemical-exchange line broadening (Figure 8). Indeed, the measure $R_{1\_max} - R_1$ shows an extraordinarily good correlation with $1 - S^2$. An excellent correlation between $R_{1\_max} - R_1$ and $1 - S^2$ was also observed in nitrogen-15 relaxation studies of BPTI (Li and Montelione, unpublished results). These observations demonstrate that the distributions of subnanosecond backbone motions in hTGFα can be described reliably using R_1 measurements alone, even in the presence of significant nitrogen-15 chemical-exchange line broadening.

It was also useful to compare values of local root-mean-squared deviations (rmsd's) of the polypeptide backbone with the relaxation parameters. Backbone atoms (N, C^α, C′) for 15 energy-refined structures of hTGFα (Moy et al., 1993) were superimposed in five residue segments, and these local rmsd values were compared with $1 - S^2$, $R_{1\_max} - R_1$, and $HNOE_{max}$ − HNOE (Figure 8). For the polypeptide segments Phe5–Asp-7 , Val-39–Gly-40, and Asp-47–Ala-50, structural disorder in the ensemble of NMR structures corresponds to portions of the molecule which exhibit internal motions on the sub-nanosecond time scale. However, the disorder in polypeptide segment Cys-8–Phe-15 of the solution NMR structures cannot be attributed to internal motions on the sub-nanosecond time scale. Although R_1 data are not available for most residues in this surface loop of hTGFα because of saturation-transfer effects, with the exception of site His-12 the PFG-HNOE data indicate no more fast internal motions in segment Cys-8–Phe-15 than in the rest of the hTGFα structure (see Figures 5C and 8D). However, several residues in this loop (e.g., Thr-13 and Phe-15) do show significant nitrogen-15 chemical-exchange line broadening (Figure 6B) attributed to slower time-scale motions. The lack of sufficient homonuclear NOE data in this surface loop of hTGFα appears therefore to be due to the combination of chemical-exchange line broadening and saturation-transfer effects. Accordingly, the poorly defined structure of polypeptide segment Cys-8–Phe-15 at neutral pH (Moy et al., 1993) can probably be improved using PFG-based NOESY experiments designed to minimize saturation-transfer effects.

Overcoming Artifacts in HNOE Measurements Due to Solvent Saturation-Transfer Effects. Measurements of ^1H–^{15}N HNOE can suffer from certain systematic errors (Kay et al., 1989; Li & Montelione, 1994). Sources of these errors include amide proton saturation periods insufficiently long for steady-state HNOE and experiment recycle times insufficiently long to provide equilibrium polarization of ^{15}N nuclei at the beginning of the pulse sequence used to record the reference spectrum. Both of these artifacts are due to the long longitudinal relaxation times of ^{15}N and generally are avoided by using a long ($>5T_1^{15N}$) amide proton saturation period in the HNOE experiment and by using a sufficiently long recycle delay to allow full ^{15}N relaxation

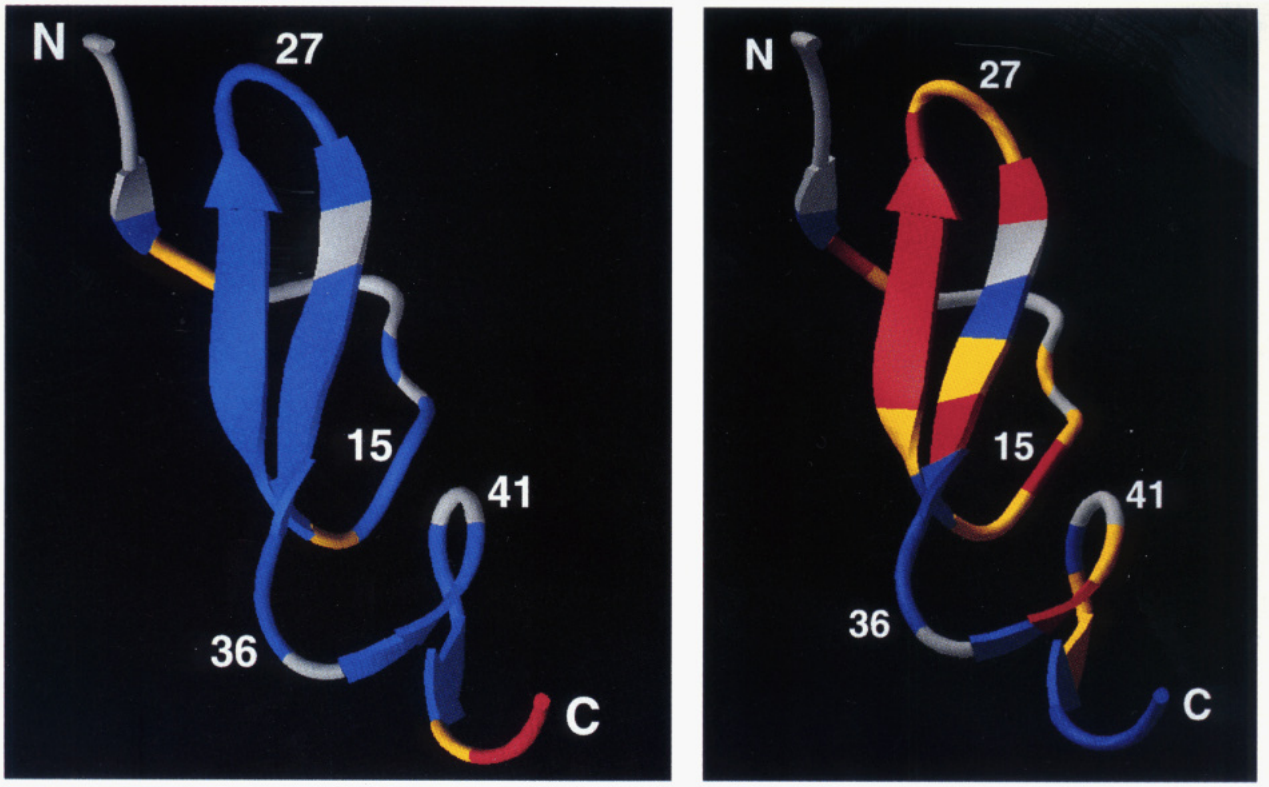

FIGURE 7: (A, left) Ribbon diagram of the solution structure of hTGFα (Moy et al., 1993) showing the polypeptide backbone color-coded according to local values of the Lipari−Szabo order parameters, S^2, at pH 7.1 and 30 °C. Backbone polypeptide segments are colored blue ($0.8 \leq S^2 \leq 1$), yellow ($0.6 \leq S^2 < 0.8$), and red ($S^2 < 0.6$), according to the estimated value of the order parameter. (B, right) Schematic representation of the solution structure of hTGFα showing backbone polypeptide segments with chemical exchange line broadening, R_{ex}, greater than 0.5 Hz. The polypeptide backbone segments are colored blue (no R_{ex} contribution or $R_{ex} < 0.5$ Hz), yellow ($0.5 \leq R_{ex} \leq 2$ Hz), and red ($R_{ex} > 2$ Hz), depending on the amount of chemical exchange line broadening indicated by the relaxation measurements. Polypeptide segments for which order parameters and other motional parameters could not be determined are shown in gray.

in the reference data set.

Another important artifact arises from saturation-transfer effects (Kay et al., 1989; Grzesiek & Bax, 1993; Li & Montelione, 1993, 1994). For protein solutions at neutral pH, chemical exchange between the amide protons and water is often sufficiently fast and the R_1 relaxation rate of amide protons sufficiently slow that saturated solvent protons can exchange into amide proton sites during the preparation period and reduce longitudinal ^{1}H magnetization. The resulting nonequilibrium polarization of amide protons results in ^{1}H−^{15}N HNOE in the reference experiment recorded without direct amide proton saturation (Kay et al., 1989). These artifacts can be minimized by using heteronuclear coherence selection with pulsed-field gradients for solvent suppression together with a recycle delay sufficiently long for the magnetization of water and any perturbations to ^{15}N polarization to relax back to equilibrium values during the preparation period (Li & Montelione, 1993, 1994). Alternatively, it is possible to flip the transverse water magnetization back onto the $+Z$ axis with properly phased frequency-selective flip-back pulses (Grzesiek & Bax, 1993). Such flip-back pulses, however, may not efficiently convert *all* transverse water magnetization back into longitudinal magnetization and also attenuate HNOE signals from amide protons with frequencies near to the water resonance. Although the use of long recycle times in the PFG-HNOE experiment (Li & Montelione, 1994) is costly in terms of instrument time, this procedure ensures circumventing artifacts associated with residual water saturation, offset effects associated with flip-back pulses, and incomplete nitrogen-15 longitudinal relaxation in these measurements.

Rapid Amide Proton Exchange. When amide protons in the reference spectrum are partially saturated by solvent saturation-transfer effects, the apparent HNOE ($HNOE_{app}$) is given by (Li & Montelione, 1994)

$$HNOE_{app} = HNOE/(1 + \alpha\eta) \qquad (15)$$

where the quantity η is the HNOE enhancement, which for ^{15}N nuclei is always <0, HNOE is the steady-state value of the heteronuclear NOE, and α is the fraction of HNOE enhancement (η) in the reference spectrum due to partial saturation of the amide proton. The value α varies between 0 (no perturbation of ^{15}N polarization due to partial saturation of the amide proton) and 1 (when the amide proton is fully saturated and results in a maximum HNOE to nitrogen). As partially saturated amide protons are relaxing while the HNOE in the reference spectrum develops, these α values reflect a time-averaged effect of partially saturated amide protons on the nitrogen-15 polarization rather than a direct measure of the fractional saturation of the amide proton. Nonetheless, they provide useful qualitative information about fast amide proton exchange and surface accessiblity (Li & Montelione, 1994).

Apparent HNOE's ($HNOE_{app}$) measured with and without weak solvent presaturation are summarized in Figure 9A, and values of α computed from these data using eq 15 are shown in Figure 9B. As expected, increased $HNOE_{app}$ amplitudes are seen in the data recorded with weak solvent presaturation. Interestingly different amide protons exhibit different degrees of saturation-transfer effect on HNOE. For example, amide nitrogens of the surface polypeptide loop

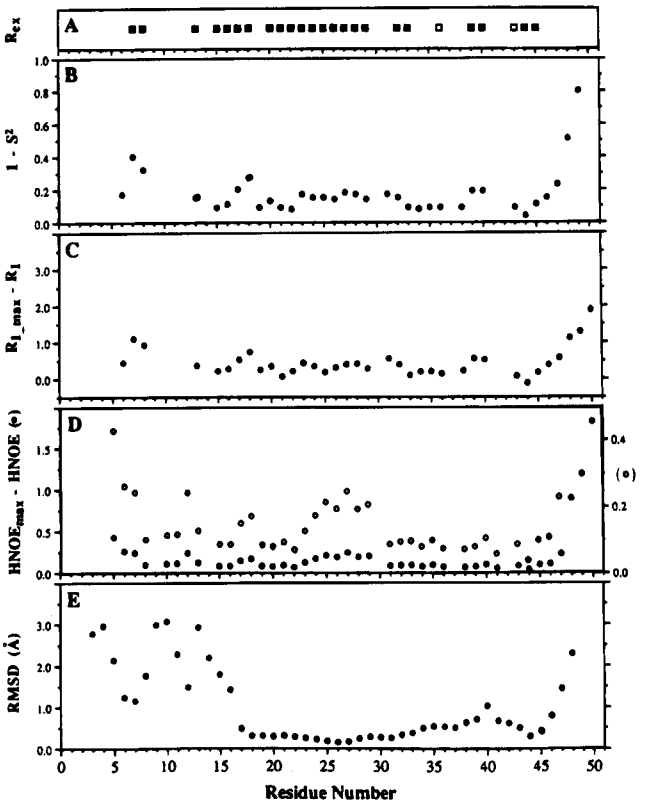

FIGURE 8: Survey of relaxation data for hTGFα at pH 7.1 and 30 °C showing (A) backbone amide sites with significant (>0.5 Hz) chemical exchange line broadening, (B) the sub-nanosecond flexibility, $1 - S^2$, (C) the attenuation in longitudinal relaxation rates due to internal motions, $R_{1\_max} - R_1$, (D) the attenuation in HNOE due to internal motions, $HNOE_{max} - HNOE$, and (E) local rmsd of backbone atomic coordinates. In panel A, residues with $R_{ex} \geq 0.5$ Hz and $0 < R_{ex} < 0.5$ Hz are represented by ■ and □, respectively. In panels C and D, R_{1_max} and $HNOE_{max}$ are calculated from theoretical functions (eqs 4 and 6, respectively) using $\tau_m = 3.76$ ns, $S^2 = 1$, an N−H bond length of 1.02 Å, and the value of the chemical shift tensor $\sigma_{||} - \sigma_{\perp} = -160$ ppm. R_1 and HNOE are the experimental data. In panel D, solid and open circles represent the values of $HNOE_{max} - HNOE$ plotted in the scale range 0−2.0 (left) and 0−0.5 (right), respectively. In panel E, the local rmsd values are obtained by superimposing the backbone atoms (N, C^{α}, C′) in five residue segments for 15 energy-refined structures of hTGFα (Moy et al., 1993).

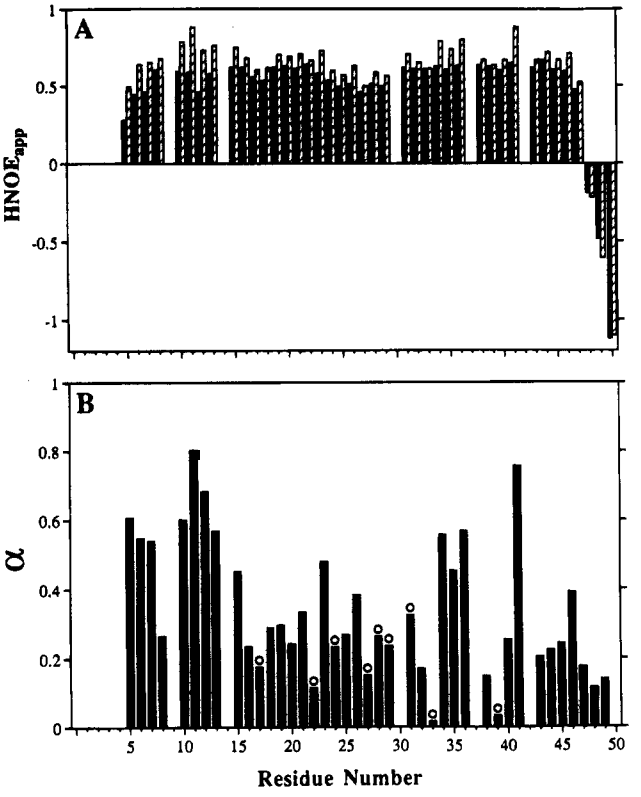

FIGURE 9: Plots of $^1H-^{15}N$ HNOE versus residue number. (A) Comparison of $^1H-^{15}N$ HNOE of hTGFα recorded with (cross-hatched □) and without (■) weak water presaturation in the reference data set without explicit amide proton saturation. Presaturation of the H_2O solvent signal was carried out for 600 ms using a power corresponding to a decoupling modulation frequency of 900 Hz. (B) Survey of the saturation-transfer effects α as a function of residue number. The backbone amide protons of the residues involving hydrogen bonds in the NMR solution structures of hTGFα at pH 6.5 (Moy et al., 1993) are indicated by open circles. Hydrogen bonds were identified using the Sybyl molecular graphics program (Tripos, Inc). The criteria for identifying a hydrogen bond between an amide donor and an acceptor atom were as follows: (i) the minimum angle formed by the donor and acceptor is 120°, and (ii) the maximum and minimum distances between the hydrogen-bonded donor and an acceptor are 2.8 and 0.8 Å, respectively. Fifteen energy-refined structures of hTGFα were analyzed, and amide protons were assigned as hydrogen-bonded if these criteria were met for more than 50% of the structures analyzed.

segment Phe-5−Phe-15 generally exhibit large α values. Amide nitrogens of residues Phe-23, Cys-34, Ser-36, and Ala-41 that are solvent-exposed in the solution structure of hTGFα also have large values of α. On the other hand, most of the amide nitrogens that are involved in intramolecular hydrogen bonds (open circles in Figure 9B) in the NMR solution structure of hTGFα have smaller α values. The fact that some amide nitrogens exhibiting small α values are not hydrogen bond donors in the available NMR structures of hTGFα suggests that such data could be used to identify additional hydrogen bond constraints and for further structure refinement.

Motional Order Parameters for hTGFα. The overall order parameter S^2 is an indicator of sub-nanosecond internal motions experienced by each backbone amide $^{15}N-^1H$ bond vector. From the plots showing distributions of S^2 values (Figures 6A and 7A), the fast time-scale internal motions of hTGFα are localized in the N- and C-terminal polypeptide segments and in a few surface β-bends (Figure 7A). The C-terminal residues, Leu-48, Leu-49, and Ala-50, are highly mobile, with small values of S^2 and negative HNOE's. Moreover, the relaxation behavior of these residues in the C-terminus is best described by models with multiple internal correlation times (e.g., model 5 of Table 1). These results indicate that the C-terminal polypeptide segment of hTGFα is very dynamic on the sub-nanosecond time scale. Conformational flexibility in this region of hTGFα was suggested from the three-dimensional solution NMR structure (Moy et al., 1993), in which the coordinates of these residues are poorly defined (see panel E of Figure 8).

Slow Internal Motions in hTGFα: Lifetimes of Conformations Associated with Slow Internal Motions. In the final analysis 23 residues exhibit ^{15}N exchange broadening greater than 0.5 Hz (Figures 6B and 7B). The observed increase in line width is directly proportional to the lifetime τ_{ex} of the exchange process and the differences in chemical shifts between the various states (Becker, 1972). Assuming two equally populated states, the observation that the chemical-exchange line broadening is not refocused in time interval $2\tau = 720$ μs between 180° pulses of the CPMG sequence indicates an upper limit for the lifetime of the chemical-

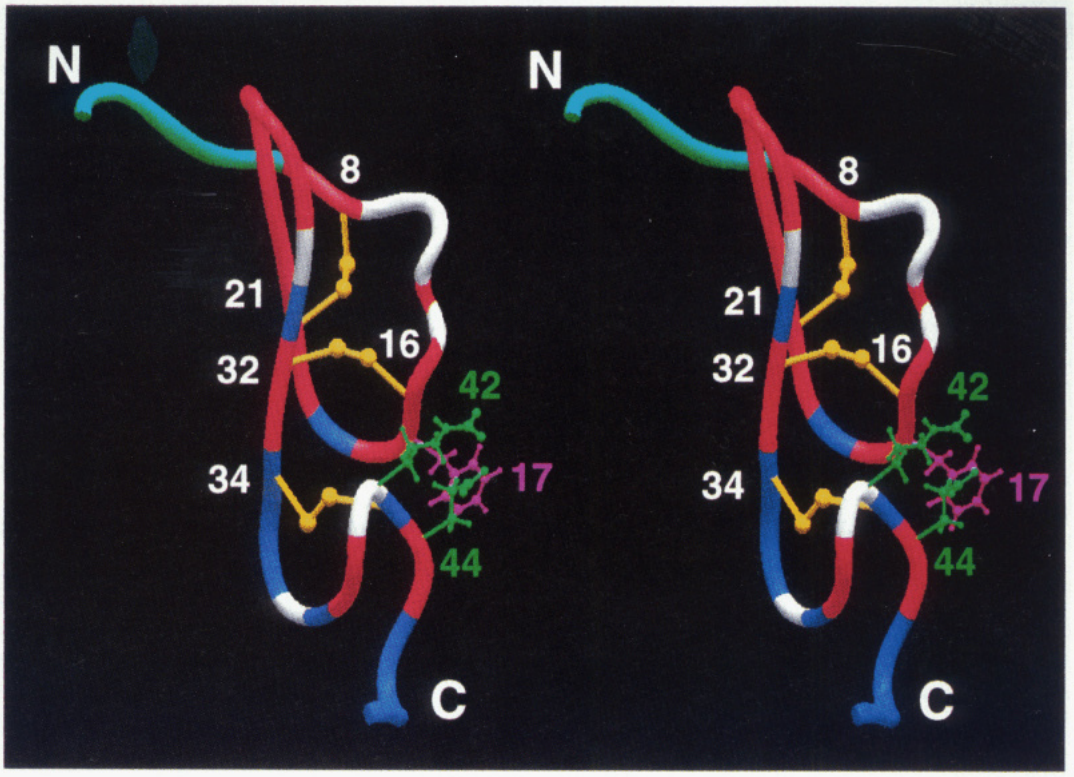

FIGURE 10: Stereo diagram of the NMR solution structure of hTGFα showing backbone polypeptide segments color-coded according to nitrogen-15 exchange line broadening, R_{ex}. Polypeptide segments are colored red ($R_{ex} \geq 0.5$ Hz) or blue (no R_{ex} contribution or $R_{ex} < 0.5$ Hz) depending on the presence or absence of chemical exchange line broadening in the extended Lipari−Szabo analysis. Backbone nitrogens for which dynamic parameters could not be calculated reliably are colored white, except for the polypeptide segment Val-1−Asn-6, which is colored blue-green to highlight the fact that it contains the first strand of the N-terminal β-sheet. Polypeptide segment Val-1−Asn-6 is thought to be in dynamic equilibrium between a conformationally disordered state and a conformation in which it is hydrogen-bonded to the central β-strand (Moy et al., 1993). Side chains are shown for three residues, Phe-17 (lavender), Arg-42 (green), and Glu-44 (green). Approximate residue locations are labeled on the structure.

exchange process of ~2.5 ms (Bloom et al., 1965; Deverell et al., 1970; Clore et al., 1990; Orekhov et al., 1994). For the same model, and assuming a maximum ^{15}N chemical shift difference of 10 ppm between the two exchanging states and a minimum detectable increase in line width of 0.5 Hz, the lower limit for the exchange lifetime τ_{ex} is calculated from standard line-shape analysis (Becker, 1972) as ~1.25 μs. Efforts to obtain more precise estimates of the lifetimes and populations of these conformational states of hTGFα from analysis of the effects of different CPMG spin-locking field strengths on the measured values of transverse relaxation rates are now in progress.

Structural Interpretation of Slow Internal Motions in hTGFα. One significant shortcoming of Lipari−Szabo analysis is that the resulting interpretation does not provide an atomic model of the underlying motions. While these relaxation time measurements provide definitive evidence for slow internal motions in hTGFα, they do not provide an molecular description of the structural dynamics. In an attempt to rationalize the distribution of nitrogen-15 chemical-exchange line broadening in the molecule, we examined the three-dimensional structure for potential sites of dynamic structural variations relative to the positions of strongly shielding functional groups such as charged and aromatic side chains (Figure 10).

Several studies (Kline et al., 1990; Harvey et al., 1991; Moy et al., 1993) have suggested that there may be a dynamic equilibrium in binding the first β-strand (Phe-5−Asn-6) of the core β-sheet with the second β-strand (Gly-19−Val-25) at neutral pH. While weak interstrand NOE's are observed, the amide hydrogen−deuterium exchange rates of these interstrand hydrogen bonds are much faster than for other interstrand hydrogen bond donors in hTGFα. Moreover, at acidic pH no NOE's are observed between these two β-strands, and the polypeptide segment Val-1−Cys-8 is highly disordered, while the major hydrogen-bonded β-sheet structures involving polypeptide segments Gly-19−Cys-34 and His-35−Asp-47 are not disturbed. Accordingly, the large chemical-exchange line broadening effects seen in polypeptide segments Asp-7−Cys-8 and Cys-21−Val-25 (see Figure 10) are consistent with a slow dynamic equilibrium between bound and free forms of the first (Phe-5−Asn-6) and second (Gly-19−Val-25) β-strands.

Another kind of internal segmental motion, hinge-bending between the two subdomains of hTGFα, has been suggested (Moy et al., 1993) from analysis of tertiary NOE's and comparisons of the distributions of these NOE's with those observed in mEGF. Many more tertiary NOE's between the N- and C-terminal subdomains are observed for mEGF than for hTGFα, resulting in three-dimensional structures which are somewhat different with respect to the relative orientations of these domains (Moy et al., 1993). It has been proposed that the relevant inter-subdomain NOE's in hTGFα are quenched or significantly line-broadened by inter-subdomain hinge-bending motions (Moy et al., 1993). Hinge-bending motions between the two subdomains are also predicted by normal mode analysis for mEGF (Ikura & Gō, 1993). As can be seen in Figures 7B and 10, many residues (Phe-15, Cys-16, Phe-17, His-18, Cys-32, Val-33, Val-39, Gly-40, Glu-44, and His-45) at the interface between the two

subdomains of hTGFα exhibit significant nitrogen-15 exchange line broadening, consistent with hinge-bending motions between the two subdomains on the microsecond time scale. In addition to the nitrogen-15 chemical-exchange broadening described here at pH 7.1, unusually broad proton line widths are observed for backbone protons of polypeptide segments Phe-15−Gly-19 and Tyr-38−Glu-44 at pH 6.5 (Moy et al., 1993). Nitrogen-15 exchange broadening in the polypeptide segment Phe-15−His-18 can be attributed to chemical shift differences arising from fluctuating electric fields at these sites from the Arg-42−Glu-44 salt bridge (Figure 10) and partially charged His-45 imidazole in the different conformational states of the inter-subdomain motion. Similarly, different ring current shifts from residue Phe-17 in these dynamic conformational states of the hinge-bending motion provide an explanation for the nitrogen-15 exchange line broadening in polypeptide segment Glu-44−His 45 (Figure 10).

Inspection of Figure 10 suggests also a third mechanism for the slow conformational processes in hTGFα, disulfide bond isomerization. Isomerization between $\chi_3 = \pm 90°$ low-energy states of disulfide bonds involves an activation energy barrier of some 6 kcal/mol (Fraser et al., 1971) and has been observed to result in chemical-exchange line broadening of nearby backbone amide nitrogens in the solution structure of BPTI (Otting et al., 1993; Szyperski et al., 1993; Li and Montelione, unpublished results). In hTGFα, the backbone amide nitrogens in nearly all of the residues flanking the Cys-8−Cys-21 and Cys-16−Cys-32 disulfide bonds, including those of polypeptide segments Asp-7−Cys-8, Phe-15−Phe-17, Thr-20−Arg-22, and Cys-32−Val-33, exhibit significant chemical-exchange line broadening (Figure 10). While all three of these explanations for the slow conformational dynamics are consistent with the experimental data, additional studies will be required to demonstrate the relative contributions of β-strand dissociation, subdomain hinge-bending motions, and disulfide bond isomerization to the slow exchange processes in hTGFα.

Implications for Understanding the Molecular Recognition Process. Comparisons of the backbone dynamics of free and bound macromolecular complexes can provide crucial information for understanding the energetics of the molecular recognition process (Akke et al., 1993a,b). Our dynamic analysis of free hTGFα provides evidence for internal motions on both sub-nanosecond and microsecond time scales. These motions are localized in several regions of the protein, including polypeptide segments Thr-13−His-18 and Val-39−Glu-44. In the native structure at neutral pH (Moy et al., 1993), these portions of hTGFα pack against one another to form an interface between the two subdomains. This interface includes two residues, Phe-15 and Arg-42, known from site-directed mutagenesis studies to be essential for receptor recognition (Defeo-Jones et al., 1988, 1989; Engler et al., 1990). This region of the related EGF molecule also includes one of its proposed receptor-binding epitopes [for a review, see Campbell and Bork (1993)]. As there is significant conformational flexibility of this putative binding region (i.e., polypeptide segments Phe-15−His-18 and Val-39−Glu-44) in the free hTGFα molecule, it is likely that changes in these internal motions make an important contribution to the free energy of EGF-receptor binding by hTGFα. However, further studies by titration calorimetry and NMR will be required in order to fully understand the role of the internal dynamics described in this paper in the molecular recognition process.

ACKNOWLEDGMENT

We thank Dr. M. Winkler and Genentech Corp. for providing the sample of hTGFα, Prof. A. Palmer for providing the relaxation analysis program MODELFREE, and both Molecular Simulations, Inc. (NMR COMPASS), and Tripos Associates, Inc. (TRIAD), for providing NMR data processing software. We also thank M. Akke, A. Arseniev, C. Biamonti, B. Celda, J. Kördel, S. Leiberman, R. Levy, A. Palmer, and Z. Shang for helpful discussions.

REFERENCES

Abragam, A. (1961) *The Principles of Nuclear Magnetism*, Clarendon Press, Oxford.

Akke, M., Brüschweiler, R., & Palmer, A. G. (1993a) *J. Am. Chem. Soc. 115*, 9832−9833.

Akke, M., Skelton, N. J., Kördel, J., Palmer, A. G., & Chazin, W. J. (1993b) *Biochemistry 32*, 9832−9844.

Anzano, M. A., Roberts, A. B., Smith, J. M., Sporn, M. B., & De Larco, J. E. (1983) *Proc. Natl. Acad. Sci. U.S.A. 80*, 6264−6268.

Baron, M., Norman, D. G., Harvey, T. S., Handford, P. A., Mayhew, M., Tse, A. G. D., Brownlee, G. G., & Campbell, I. D. (1992) *Protein Sci. 1*, 81−90.

Becker, E. D. (1972) *High Resolution NMR: Theory and Chemical Applications*, Academic Press, New York.

Bloom, M., Reeves, L. W., & Wells, E. J. (1965) *J. Chem. Phys. 42*, 1615−1624.

Boyd, J., Hommel, U., & Campbell, I. D. (1990) *Chem. Phys. Lett. 175*, 477−482.

Brown, C. S., Mueller, L., & Jeffs, P. W. (1989) *Biochemistry 28*, 593−599.

Burgess, A. W. (1989) *Brit. Med. Bull. 45*, 401−424.

Campbell, I. D., & Bork, P. (1993) *Curr. Opin. Struct. Biol. 3*, 385−392.

Cantor, C. R., & Schimmel, P. R. (1980) *Biophysical Chemistry*, Freeman, San Francisco.

Carpenter, G., Stoscheck, C. M., Preston, Y. A., & De Larco, J. E. (1983) *Proc. Natl. Acad. Sci. U.S.A. 80*, 5627−5630.

Carr, H. Y., & Purcell, E. M. (1954) *Phys. Rev. 94*, 630−638.

Carver, J. A., Cooke, R. M., Esposito, G., Campbell, I. D., Gregory, H., & Sheard, B. (1986) *FEBS Lett. 205*, 77−81.

Clore, G. M., Szabo, A., Bax, A., Kay, L. E., Driscoll, P. C., & Gronenborn, A. M. (1990a) *J. Am. Chem. Soc. 112*, 4989−4991.

Clore, G. M., Driscoll, P. C., Wingfield, P. T., & Gronenborn, A. M. (1990b) *Biochemistry 29*, 7387−7401.

Cooke, R. M., Wilkinson, A. J., Baron, M., Pastore, A., Tappin, M. J., Campbell, I. D., Gregory, H., & Sheard, B. (1987) *Nature 327*, 339−341.

Defeo-Jones, D., Tai, J. Y., Wegrzyn, R. J., Vuocolo, G. A., Baker, A. E., Payne, L. S., Garsky, V. M., Oliff, A., & Rieman, M. W. (1988) *Mol. Cell. Biol. 8*, 2999−3007.

Defeo-Jones, D., Tai, J. Y., Vuocolo, G. A., Wegrzyn, R. J., Shofield, T. L., Rieman, M. W., & Oliff, A. (1989) *Mol. Cell. Biol. 9*, 4083−4086.

Derynck, R., Roberts, A. B., Winkler, M. E., Chen, E. Y., & Goeddel, D. V. (1984) *Cell 38*, 287−297.

Deverell, C., Morgan, R. E., & Strange, J. H. (1970) *Mol. Phys. 18*, 553−559.

Engler, D. A., Montelione, G. T., & Niyogi, S. K. (1990) *FEBS Lett. 271*, 47−50.

Fraser, R. R., Boussard, G., Saunders, J. K., Lambert, J. B., & Mixan, C. E. (1971) *J. Am. Chem. Soc. 93*, 3822−3823.

Graves, B. J., Crowther, R. L., Chandran, C., Rumberger, J. M., Li, S., Huang, K.-S., Presky, D. H., Familletti, P. C., Wolitzky, B. A., & Burns, D. K. (1994) *Nature 367*, 532−538.

Grzesiek, S., & Bax, A. (1993) *J. Am. Chem. Soc. 115*, 12593−12594.

Guerin, M., Gabillot, M., Mathieu, M.-C., Travagli, J.-P., Spielmenn, M., Andrieu, N., & Riou, G. (1989) *Int. J. Cancer 43*, 201−208.
Hansen, A. P., Petros, A. M., Meadows, R. P., Nettesheim, D. G., Mazar, A. P., Olejniczak, E. T., Xu, R. X., Pederson, T. M., Henkin, J., & Fesik, S. W. (1994) *Biochemistry 33*, 4847−4864.
Harris, W. E., & Kratochvil, B. (1981) *An Introduction to Chemical Analysis*, Saunders College Publishing, New York.
Harvey, T. S., Wilkinson, A. J., Tappin, M. J., Cooke, R. M., & Campbell, I. D. (1991) *Eur. J. Biochem. 198*, 555−562.
Hiyama, Y., Niu, C., Silverton, J. V., Bavoso, A., & Torchia, D. A. (1988) *J. Am. Chem. Soc. 110*, 2378−2383.
Hommel, U., Harvey, T. S., Driscoll, P. C., & Campbell, I. D. (1992) *J. Mol. Biol. 227*, 271−282.
Huang, L. H., Cheng, H., Pardi, A., Tam, J. P., & Sweeney, W. V. (1991) *Biochemistry 30*, 7402−7409.
Ikura, T., & Gō, N. (1993) *Proteins 16*, 423−436.
Jyung, R. W., & Mustoe, T. A. (1992) in *Clinical Applications of Cytokines* (Gearing, A., Rossio, J., & Oppenheimer, J., Eds.) Oxford University Press, Oxford.
Kay, L. E., Torchia, D. A., & Bax, A. (1989) *Biochemistry 28*, 8972−8979.
Kay, L. E., Nicholson, L. K., Delaglio, F., Bax, A., & Torchia, D. A. (1992) *J. Magn. Reson. 97*, 359−375.
Kline, T. P., Brown, F. K., Brown, S. C., Jeffs, P. W., Kopple, K. D., & Mueller, L. (1990) *Biochemistry 29*, 7805−7813.
Kohda, D., & Inagaki, F. (1988) *J. Biochem. (Tokyo) 103*, 554−571.
Kohda, D., & Inagaki, F. (1992a) *Biochemistry 31*, 11928−11939.
Kohda, D., & Inagaki, F. (1992b) *Biochemistry 31*, 677−685.
Kohda, D., Gō, N., Hayashi, K., & Inagaki, F. (1988) *J. Biochem. (Tokyo) 103*, 741−743.
Kohda, D., Shimada, I., Miyake, T., Fuwa, T., & Inagaki, F. (1989) *Biochemistry 28*, 953−958.
Kördel, J., Skelton, N. J., Palmer, A. G., & Chazin, W. J. (1992) *Biochemistry 31*, 4856−4866.
Li, Y.-C., & Montelione, G. T. (1993) *J. Magn. Reson B101*, 315−319.
Li, Y.-C., & Montelione, G. T. (1994) *J. Magn. Reson. B105*, 45−51.
Lipari, G., & Szabo, A. (1982a) *J. Am. Chem. Soc. 104*, 4546−4559.
Lipari, G., & Szabo, A. (1982b) *J. Am. Chem. Soc. 104*, 4559−4570.
Marion, D., & Wüthrich, K. (1983) *Biochem. Biophys. Res. Commun. 113*, 967−974.
Marquardt, H., Hunkapiller, M. W., Hood, L. E., Twardzik, D. R., De Larco, J. E., Stephenson, J. R., & Todaro, G. J. (1983) *Proc. Natl. Acad. Sci. U.S.A. 80*, 4684−4688.
Mayo, K. H., Cavalli, R. C., Peters, A. R., Boelens, R., & Kaptein, R. (1989) *Biochem. J. 257*, 197−205.
Meiboom, S., & Gill, D. (1958) *Rev. Sci. Instrum. 29*, 688−691.
Montelione, G. T., Wüthrich, K., Nice, E. C., Burgess, A. W., & Scheraga, H. A. (1986) *Proc. Natl. Acad. Sci. U.S.A. 83*, 8594−8598.
Montelione, G. T., Wüthrich, K., Nice, E. C., Burgess, A. W., & Scheraga, H. A. (1987) *Proc. Natl. Acad. Sci. U.S.A. 84*, 5226−5230.
Montelione, G. T., Wüthrich, K., & Scheraga, H. A. (1988) *Biochemistry 27*, 2235−2243.
Montelione, G. T., Winkler, M. E., Burton, L. E., Rinderknecht, E., Sporn, M. B., & Wagner, G. (1989) *Proc. Natl. Acad. Sci. U.S.A. 86*, 1519−1523.
Montelione, G. T., Wüthrich, K., Burgess, A. W., Nice, E. C., Wagner, G., Gibson, K. D., & Scheraga, H. A. (1992) *Biochemistry 31*, 236−249.
Moy, F. J., Li, Y.-C., Rauenbuehler, P., Winkler, M. E., Scheraga, H. A., & Montelione, G. T. (1993) *Biochemistry 32*, 7334−7353.
Nagayama, K. (1986) *J. Magn. Reson. 66*, 240−249.
Orekhov, V. Y., Pervushin, K. V., & Arseniev, A. S. (1994) *Eur. J. Biochem. 219*, 887−896.
Otting, G., Liepinsh, E., & Wüthrich, K. (1993) *Biochemistry 32*, 3571−3582.
Padmanabhan, K., Padmanabhan, K. P., Tulinsky, A., Park, C. H., Bode, W., Huber, R., Blankenship, D. T., Cardin, A. D., & Kisiel, W. (1993) *J. Mol. Biol. 232*, 947−966.
Palmer, A. G., Rance, M., & Wright, P. E. (1991) *J. Am. Chem. Soc. 113*, 4371−4380.
Palmer, A. G., Skelton, N. J., Chazin, W. J., Wright, P. E., & Rance, M. (1992) *Mol. Phys. 75*, 699−711.
Peng, J. W., & Wagner, G. (1992) *Biochemistry 31*, 8573−8586.
Powers, R., Clore, G. M., Stahl, S. J., Wingfield, P. T., & Gronenborn, A. (1992) *Biochemistry 31*, 9150−9157.
Press, W. H., Flannery, B. P., Teukolsky, S. A., & Vetterling, W. T. (1986) *Numerical Recipes*, Cambridge University Press, Cambridge.
Roberts, A. B., Lamb, L. C., Newton, D. L., Sporn, M. B., De Larco, J. E., & Todaro, G. J. (1980) *Proc. Natl. Acad. Sci. U.S.A. 77*, 3494−3498.
Roberts, A. B., Anzano, M. A., Lamb, L. C., Smith, J. M., & Sporn, M. B. (1981) *Proc. Natl. Acad. Sci. U.S.A. 78*, 5339−5343.
Selander, M., Persson, E., Stenflo, J., & Drakenberg, T. (1990) *Biochemistry 29*, 8111−8118.
Shaka, A. J., Barker, P. B., & Freeman, R. (1985) *J. Magn. Reson. 64*, 547−552.
Simpson, R. J., Smith, J. A., Moritz, R. L., O'Hare, M. J., Rudland, P. S., Morrison, J. R., Lloyd, C. J., Grego, B., Burgess, A. W., & Nice, E. C. (1985) *Eur. J. Biochem. 153*, 629−637.
Smith, B. O., Downing, A. K., Dudgeon, T. J., Cunningham, M., Driscoll, P. C., & Campbell, I. D. (1994) *Biochemistry 33*, 2422−2429.
Stone, M. J., Fairbrother, W. J., Palmer, A. G., Reizer, J., Saier, M. H., & Wright, P. E. (1992) *Biochemistry 31*, 4394−4406.
Szyperski, T., Luginbühl, P., Otting, G., Güntert, P., & Wüthrich, K. (1993) *J. Biomol. NMR 3*, 151−164.
Tappin, M. J., Cooke, R. M., Fitton, J. E., & Campbell, I. D. (1989) *Eur. J. Biochem. 179*, 629−637.
Ullner, M., Selander, M., Persson, E., Stenflo, J., Drakenberg, T., & Teleman, O. (1992) *Biochemistry 31*, 5974−5983.
Weis, W. I. (1994) *Structure 2*, 147−150.

BI941806C